

TOPOLOGICAL LEARNING FOR BRAIN NETWORKS

BY TANANUN SONGDECHAKRAIWUT^a AND MOO K. CHUNG^b

Department of Biostatistics and Medical Informatics, University of Wisconsin–Madison, ^asongdechakra@wisc.edu, ^bmkchung@wisc.edu

This paper proposes a novel topological learning framework that integrates networks of different sizes and topology through persistent homology. Such challenging task is made possible through the introduction of a computationally efficient topological loss. The use of the proposed loss bypasses the intrinsic computational bottleneck associated with matching networks. We validate the method in extensive statistical simulations to assess its effectiveness when discriminating networks with different topology. The method is further demonstrated in a twin brain imaging study where we determine if brain networks are genetically heritable. The challenge here is due to the difficulty of overlaying the topologically different functional brain networks obtained from resting-state functional MRI onto the template structural brain network obtained through diffusion MRI.

1. Introduction. Network analysis has experienced tremendous advances in the last few decades. Networks are often represented using graphs consisting of nodes and edges. In standard network analysis the focus is mainly on analyzing how data at nodes are interacting with each other. Strength of the interaction is represented as edge weights. In social science, human interactions are modeled by viewing humans as nodes and human interaction as edges (Scott (1988)). In molecular studies, interatomic distances in a molecule are measured across atoms and serve as edge weights while the atoms themselves serve as nodes (Chung and Ombao (2021), Xia and Wei (2014)). In brain imaging studies, the whole brain is parcellated into hundreds of disjoint regions, which then serve as nodes, while brain activities between parcellations based on correlations serve as edge weights (Arslan et al. (2018), Desikan et al. (2006), Fornito, Zalesky and Bullmore (2016), Hagmann et al. (2007), Tzourio-Mazoyer et al. (2002)).

In graph theory based network analyses (Sporns (2003), Wijk, Stam and Daffertshofer (2010)), graph theory features, such as node degrees and clustering coefficients, are often obtained from adjacency matrices after thresholding edge weights. The final statistical results may be different depending on the threshold choice (Lee et al. (2012)). This motivates the development of a multiscale network model that provides consistent results and interpretation regardless of the choice of thresholding. Topological data analysis (TDA) (Edelsbrunner, Letscher and Zomorodian (2000), Wasserman (2018)), a general framework based on algebraic topology, can provide a novel solution to the multiscale network analysis challenge. Instead of examining networks using graphs at one fixed scale, the persistent homology technique in TDA identifies persistent topological features that are robust across scales.

Numerous TDA studies have been applied to increasingly diverse biomedical problems, such as genetics (Chung et al. (2017b, 2019b)), epileptic seizure detection (Wang, Ombao and Chung (2018)), sexual dimorphism in the human brain (Songdechakraiwt and Chung (2020)), analysis of brain arteries (Bendich et al. (2016)), image segmentation (Clough et al. (2019)), image classification (Chen et al. (2019), Reininghaus et al. (2015), Singh et al.

Received December 2020; revised March 2022.

Key words and phrases. Topological data analysis, persistent homology, topological learning, Wasserstein distance, birth-death decomposition, twin brain imaging study.

(2014)), clinical predictive model (Crawford et al. (2020)) and persistence-based clustering (Chazal et al. (2013)).

Persistent homology has emerged as a powerful mathematical representation for understanding, characterizing and quantifying topology of networks. In persistent homology topological features are measured across different spatial resolutions. As the resolution changes, such features are born and die. Persistent homology associates the lifetime to these features in the form of 1D intervals from birth to death. The collection of such intervals is summarized as a *barcode* that characterizes the topology of underlying data (Ghrist (2008)). Long-lived barcodes persist over a long range of resolutions and are considered as signal (Carlsson (2009)). Recent work proposed *topological loss* that penalizes barcodes for image segmentation problem (Hu et al. (2019)). While this approach allows to incorporate topological information into the segmentation problem, the method has been limited to image segmentation with a small number of topological features due to its expensive optimization process involving $O(|V|^6)$ runtime with $|V|$ number of nodes (Edmonds and Karp (1972), Kerber, Morozov and Nigmatov (2017)). Barcodes are typically computed at a finite set of prespecified resolutions. A sufficient number of such resolutions is required to give a reasonably accurate estimation of barcodes, which quickly increases computational complexity as the size of data increases (Chung et al. (2019a), Hu et al. (2019)). This is impractical in brain networks with a far larger number of topological features involving hundreds of connected components and thousands of cycles. In this paper we propose a more principled approach that learns the topological structure of brain networks with a large number of topological features in $O(|E| \log |V|)$ runtime with $|E|$ number of edges and $|V|$ number of nodes. The proposed method bypasses the intrinsic computational bottleneck and thus enables us to perform various topology computations and optimizations at every resolution.

We illustrate the proposed method using the resting-state functional MRI (fMRI) of 194 twin pairs from the Human Connectome Project (HCP) (Van Essen et al. (2012), Van Essen et al. (2013)). HCP twin brain imaging data is considered as the *gold standard*, where the zygosity is confirmed by the blood and saliva test (Gritsenko, Lindquist and Chung (2020)). Monozygotic (MZ) twins share 100% of genes while dizygotic (DZ) twins share 50% of genes (Falconer and Mackay (1995)). MZ-twins are more similar or concordant than DZ-twins for cognitive aging, cognitive dysfunction and Alzheimer's disease (Reynolds and Phillips (2015)). These genetic differences allow us to pull apart and examine genetic and environmental influences easily *in vivo*. The differences between MZ- and DZ-twins quantify the extent to which phenotypes are influenced by genetic factors. If MZ-twins show more similarity on a given trait compared to DZ-twins, this provides evidence that genes significantly influence that trait. Previous twin brain imaging studies mainly used univariate imaging phenotypes, such as brain cortical thickness (McKay et al. (2014)), fractional anisotropy (Chiang et al. (2011)) and functional activation (Blokland et al. (2011), Glahn et al. (2010), Smit et al. (2008)), when determining heritability in a few regions of interest. Compared to prior studies on univariate imaging phenotypes, there are not many studies on the heritability of the whole brain functional networks (Blokland et al. (2011)). Measures of network topology may be worth investigating as intermediate phenotypes that indicate the genetic risk for a neuropsychiatric disorder (Bullmore and Sporns (2009)). However, the brain network analysis has not yet been adapted for this purpose beyond a small number of regions. Determining the extent of heritability of the whole brain networks is the first necessary prerequisite for identifying network-based endophenotypes. We employ our method to determine the heritability of brain networks constructed by topologically overlaying functional brain networks from fMRI onto the template structural brain network from diffusion MRI (dMRI). Our method is demonstrated to increase the sensitivity to subtle genetic signals.

2. Methods.

2.1. *Preliminary.* Consider a complete network, represented as a graph $G = (V, w)$, comprising a set of nodes V and unique positive symmetric edge weights $w = (w_{ij})$ satisfying $w_{ij} = w_{ji}$. Note that the method proposed in this paper is *translation invariant* so any negative edge weights can be made positive by translations. In addition, the condition of having unique edge weights is not restrictive in practice. Assuming edge weights follow some continuous distribution, the probability of any two edge weights being equal is zero. This is particularly true in functional brain networks where edge weights are given as the Pearson correlation between time series of brain activity (Fornito, Zalesky and Bullmore (2016)). In the case of equal edge weights, we can add infinitesimal noise and break the tie. Since the proposed method is based on the Wasserstein distance, which enjoys the stability theorem (Cohen-Steiner et al. (2010)), adding the infinitesimal noise will not affect the final numerical outcome.

The cardinality of sets is denoted using $|\cdot|$. The number of nodes and edges are then denoted as $|V|$ and $|E|$. Since G is a complete graph, we have $|E| = |V|(|V| - 1)/2$. Any incomplete graph can be treated as a special case of a complete graph with zero weights. Then, we can add infinitesimal noise to those zero weights to break ties. We emphasize that the proposed method works for arbitrary graphs. However, assuming the graph to be complete with unique positive edge weights makes exposition of the method straightforward.

The binary graph $G_\epsilon = (V, w_\epsilon)$ of G is defined as a graph consisting of the node set V and binary edge weights w_ϵ given by

$$w_\epsilon = (w_{\epsilon,ij}) = \begin{cases} 1 & \text{if } w_{ij} > \epsilon; \\ 0 & \text{otherwise.} \end{cases}$$

A *graph filtration* of G is defined as a collection of nested binary networks (Lee et al. (2012))

$$G_{\epsilon_0} \supset G_{\epsilon_1} \supset \dots \supset G_{\epsilon_k},$$

where $\epsilon_0 < \epsilon_1 < \dots < \epsilon_k$ are called filtration values. Figure 1 displays an example of the graph filtration on a four-node network.

In persistent homology a zero-dimensional topological feature is a *connected component*, which is a set of nodes and edges that are connected to each other by paths. In Figure 1 there is

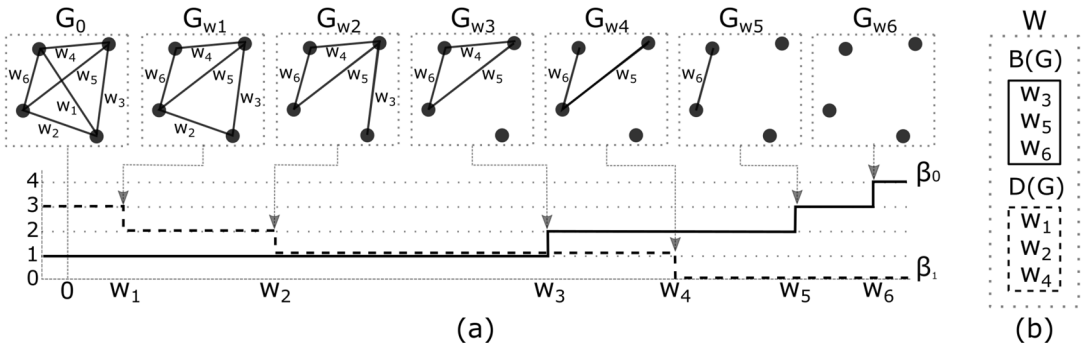


FIG. 1. (a) Graph filtration on a four-node network G . β_0 is monotonically increasing while β_1 is monotonically decreasing over the graph filtration. Connected components are born at the edge weights w_3, w_5, w_6 while cycles die at the edge weights w_1, w_2, w_4 . A cycle consisting of w_4, w_5, w_6 persists longer than any other 1D features and is considered as a topological signal. 0D barcode $\{(-\infty, \infty), (w_3, \infty), (w_5, \infty), (w_6, \infty)\}$ is represented using the birth values as $I_0(G) = \{w_3, w_5, w_6\}$. 1D barcode $\{(-\infty, w_1), (-\infty, w_2), (-\infty, w_4)\}$ is represented using the death values as $I_1(G) = \{w_1, w_2, w_4\}$. (b) We can show that 0D and 1D barcodes uniquely partition the edge weight set as $W = I_0(G) \cup I_1(G)$ with $I_0(G) \cap I_1(G) = \emptyset$.

only one connected component in graph G_0 , since all nodes and edges are connected through paths, while G_{w_6} has four connected components because each of the four nodes cannot be reached from the others by any path. The number of connected components is called the 0th Betti number β_0 , and we write $\beta_0(G_0) = 1$ and $\beta_0(G_{w_6}) = 4$.

The one-dimensional topological feature is a loop or *cycle*, which is a path that starts and ends at the same node but no other nodes in the path are overlapping. In G_{w_3} , there is one cycle consisting of edges w_4, w_5 and w_6 . The cycle can be algebraically represented as $[w_4] + [w_5] + [w_6]$ with the convention of putting clockwise orientation along the edges. In G_{w_1} , there are three cycles consisting of $[w_4] + [w_5] + [w_6]$, $-[w_5] + [w_3] + [w_2]$ and $[w_4] + [w_3] + [w_2] + [w_6]$. However, they are linearly dependent in a sense that the cycle consisting of four nodes can be written as the sum of the two other smaller cycles

$$[w_4] + [w_3] + [w_2] + [w_6] = ([w_4] + [w_5] + [w_6]) + (-[w_5] + [w_3] + [w_2]).$$

Thus, there are only two algebraically independent cycles in G_{w_1} . The total number of independent cycles is the first Betti number β_1 . We write $\beta_1(G_{w_3}) = 1$ and $\beta_1(G_{w_1}) = 2$. During the graph filtration, β_0 is monotonically increasing while β_1 is monotonically decreasing (Chung et al. (2019b)). Unlike Rips complexes (Ghrist (2008)), which are often used in persistent homology, there are no more higher-dimensional topological features than 0D and 1D.

Persistent homology keeps track of appearances (birth) and disappearances (death) of connected components and cycles over the filtration as well as their *persistence* (the duration from birth to death). Longer persistence indicates the presence of larger topological signal (Edelsbrunner and Harer (2008)). The persistence of topological features are algebraically represented as the collection of intervals (ϵ_b, ϵ_d) , where a feature appears at the filtration value ϵ_b and vanishes at the filtration value ϵ_d . The collection of such intervals is called a *barcode* (Adler et al. (2010), Ghrist (2008), Songdechakruiwut, Shen and Chung (2021)).

2.2. Birth-death decomposition. During the graph filtration, once a connected component is born, it never dies. Thus, every connected component has a death value at ∞ . We can safely discard ∞ and characterize the *0D barcode* for connected components using their birth values

$$I_0(G) : \quad \epsilon_{b1} < \epsilon_{b2} < \dots < \epsilon_{bm_0},$$

where $m_0 = \beta_0(G_\infty) - 1 = |V| - 1$. $I_0(G)$ forms the maximum spanning tree (MST) of G (Lee et al. (2012)). Cycles in the graph filtration are all considered born at $-\infty$. Thus, we can also discard $-\infty$ and characterize the *1D barcode* for cycles using their death values

$$I_1(G) : \quad \epsilon_{d1} < \epsilon_{d2} < \dots < \epsilon_{dm_1},$$

where $m_1 = \beta_1(G_0) = (|V| - 1)(|V| - 2)/2$. Removing edge w_{ij} in the graph filtration results in either the birth of a connected component or the death of a cycle. The birth of a connected component and the death of a cycle cannot possibly happen at the same time. Thus, every edge weight must be in either 0D barcode or 1D barcode, but not both (Figure 1(b)).

THEOREM 1. *The birth set $I_0(G)$ and death set $I_1(G)$ partition the edge weight set W such that $W = I_0(G) \cup I_1(G)$ with $I_0(G) \cap I_1(G) = \emptyset$. The cardinalities of $I_0(G)$ and $I_1(G)$ are $|V| - 1$ and $(|V| - 1)(|V| - 2)/2$, respectively. Furthermore, $I_0(G)$ is MST of G , and $I_1(G)$ is the remaining non-MST edge weights.*

Theorem 1 is a nontrivial statement and used in the development of our proposed topological learning framework.

2.3. *Topological loss.* Since network topology is completely characterized by 0D and 1D barcodes, the topological similarity between two networks can be measured using the difference between such barcodes. We will modify Wasserstein distance to quantify the barcode difference for the graph filtration (Clough et al. (2019), Cohen-Steiner et al. (2010), Hu et al. (2019), Kolouri et al. (2019), Rabin et al. (2011)) as follows.

Let $\Theta = (V^\Theta, w^\Theta)$ and $P = (V^P, w^P)$ be two given networks. For now, we will assume that the two networks have the same size $|V^\Theta| = |V^P|$. The case $|V^\Theta| \neq |V^P|$ will be explained in Section 2.4. The 2-Wasserstein distance between 0D barcodes is given by

$$(1) \quad \mathcal{L}_{0D}(\Theta, P) = \min_{\tau_0} \sum_{\epsilon_b \in I_0(\Theta)} [\epsilon_b - \tau_0(\epsilon_b)]^2,$$

where τ_0 is a bijection from birth sets $I_0(\Theta)$ to $I_0(P)$. $\mathcal{L}_{0D}(\Theta, P)$ is termed *0D topological loss* that measures the topological dissimilarity between networks Θ and P in terms of 0D features (connected components). Recall that the death values of all connected components in networks are ∞ . Thus, the 0D topological loss given in (1) simply ignores the death values. Even if we replace ∞ with a sufficiently large number, the loss will not be affected.

Similarly, the 2-Wasserstein distance between 1D barcodes is given by

$$(2) \quad \mathcal{L}_{1D}(\Theta, P) = \min_{\tau_1} \sum_{\epsilon_d \in I_1(\Theta)} [\epsilon_d - \tau_1(\epsilon_d)]^2,$$

where τ_1 is a bijection from death sets $I_1(\Theta)$ to $I_1(P)$. $\mathcal{L}_{1D}(\Theta, P)$, termed *1D topological loss*, measures the topological dissimilarity between networks Θ and P in terms of cycles. Again, recall that the birth values of all cycles are $-\infty$. Thus, the 1D topological loss, given in (2), simply ignores the birth values. Replacing $-\infty$ by a sufficiently small number will not affect the loss.

Instead of trying to determine the 0D and 1D topological differences separately, we want a single summary statistic measuring the overall topological differences. This can be achieved by combining the 0D and 1D topological losses as

$$\mathcal{L}_{\text{top}}(\Theta, P) = \mathcal{L}_{0D}(\Theta, P) + \mathcal{L}_{1D}(\Theta, P).$$

The 0D and 1D topological losses are variants of the *assignment problem*, which is typically solved using the cubic-time Hungarian algorithm (Edmonds and Karp (1972)). However, for the graph filtration the 0D and 1D losses have closed-form expressions that can be efficiently computed in $O(|I_0(\Theta)| \log |I_0(\Theta)|)$ and $O(|I_1(\Theta)| \log |I_1(\Theta)|)$ time, respectively, as follows.

THEOREM 2. *For the 0D topological loss we have*

$$\mathcal{L}_{0D}(\Theta, P) = \min_{\tau_0} \sum_{\epsilon_b \in I_0(\Theta)} [\epsilon_b - \tau_0(\epsilon_b)]^2 = \sum_{\epsilon_b \in I_0(\Theta)} [\epsilon_b - \tau_0^*(\epsilon_b)]^2,$$

where τ_0^* maps the i th smallest birth value in $I_0(\Theta)$ to the i th smallest birth value in $I_0(P)$ for all i . Similarly, for the 1D topological loss we also have

$$\mathcal{L}_{1D}(\Theta, P) = \min_{\tau_1} \sum_{\epsilon_d \in I_1(\Theta)} [\epsilon_d - \tau_1(\epsilon_d)]^2 = \sum_{\epsilon_d \in I_1(\Theta)} [\epsilon_d - \tau_1^*(\epsilon_d)]^2,$$

where τ_1^* maps the i th smallest death value in $I_1(\Theta)$ to the i th smallest death value in $I_1(P)$ for all i .

The minimizations in Theorem 2 are equivalent to the following assignment problem. For monotonic sequences

$$a_1 < a_2 < \dots < a_n, \quad b_1 < b_2 < \dots < b_n,$$

we consider finding $\min_{\tau} \sum_{i=1}^n (a_i - \tau(a_i))^2$ over all possible bijections τ . The optimal bijection is simply given by the identity permutation $\tau(a_i) = b_i$ and is proved by induction (Songdechakraiwt, Shen and Chung (2021)). The problem statement can be extended to a more general assignment problem between different numbers of data

$$a_1 < a_2 < \dots < a_m, \quad b_1 < b_2 < \dots < b_n.$$

In this case, however, the analytical solutions given in Theorem 2 are not applicable. The mismatching issue is discussed next.

2.4. *Topological loss between networks of different sizes.* Let $\Theta = (V^{\Theta}, w^{\Theta})$ and $P = (V^P, w^P)$ be networks of different sizes such that $|V^{\Theta}| \neq |V^P|$. There is no bijection between the birth sets and between the death sets due to the mismatching issue. This problem is often addressed through data augmentation or empirical distribution methods (Bonneel et al. (2015), Carriere, Cuturi and Oudot (2017), Deshpande, Zhang and Schwing (2018), Karras et al. (2018), Kolouri et al. (2017), Liutkus et al. (2019)). Data augmentation is probably the most popular technique for mismatches between topological features (Hu et al. (2019)), trees (Guo and Srivastava (2020)) and point sets (Chung et al. (2019b), Edelsbrunner and Harer (2008), Ghrist (2008), Patrangenaru et al. (2019), Robins and Turner (2016), Xia and Wei (2014)). An alternative approach is to express the topological loss in terms of empirical distribution functions (Bonneel et al. (2015), Carriere, Cuturi and Oudot (2017), Deshpande, Zhang and Schwing (2018), Karras et al. (2018), Kolouri et al. (2017), Liutkus et al. (2019)). The empirical distributions for birth sets of Θ and P are given by

$$\widehat{F}_{\Theta}(x) = \frac{1}{|I_0(\Theta)|} \sum_{\epsilon_b \in I_0(\Theta)} \mathbb{1}_{\epsilon_b \leq x},$$

$$\widehat{F}_P(x) = \frac{1}{|I_0(P)|} \sum_{\epsilon_b \in I_0(P)} \mathbb{1}_{\epsilon_b \leq x},$$

where $\mathbb{1}_{\epsilon_b \leq x}$ is the indicator having the value 1 if $\epsilon_b \leq x$ and the value 0 otherwise. Their pseudoinverses $F_{\Theta}^{-1}(z)$ and $F_P^{-1}(z)$ are defined as the smallest x for which $\widehat{F}_{\Theta}(x) \geq z$ and $\widehat{F}_P(x) \geq z$. Then, 0D topological loss is given by (Kolouri et al. (2017))

$$(3) \quad \mathcal{L}_{0D}(\Theta, P) = \int_0^1 (\widehat{F}_{\Theta}^{-1}(x) - \widehat{F}_P^{-1}(x))^2 dx.$$

Similarly, 1D topological loss can be defined in terms of the empirical distribution for death sets. We can efficiently compute the loss between networks of different sizes by computing the integral numerically (Songdechakraiwt et al. (2022a)). In addition, when the network sizes are equal, the empirical distributions are still well defined, and the loss given in (3) exactly matches our analytical expression in Theorem 2.

In actual brain imaging applications, brain networks are usually constructed following standard pipelines resulting in networks with the same number of nodes (Fornito, Zalesky and Bullmore (2016), Sporns (2003)). Thus, matching brain networks of different sizes can be avoided, and there is no need to augment data or use empirical distributions. Comparing the two techniques, when the numerical accuracy relative to the definition of the Wasserstein distance is important, the data augmentation approach will not provide a relatively accurate distance. In such cases, the empirical distribution approach is preferable. Apart from the two major techniques for handling networks of different sizes, there are other available methods (Deshpande, Zhang and Schwing (2018), Karras et al. (2018)). In particular, Marchese and Maroulas (2018) proposed a variant of the Wasserstein distance that explicitly penalizes cardinality and short-lived persistence points and showed that the variant can utilize geometric information to improve the discriminative power in classification.

2.5. *Topological learning.* There are previous attempts to incorporate topology into learning and inference frameworks. Adler, Agami and Pranav (2017) proposed the parametric model for persistence diagrams based on Gibbs distribution and developed modeling, replication and inference procedures. Marchese and Maroulas (2018) built the probability measure on the metric space of persistence diagrams used in classifying signals. In (Maroulas, Nasrin and Oballe (2020)), Bayesian framework was developed by modeling persistence diagrams as a Poisson point process. Naitzat, Zhitnikov and Lim (2020) investigated how Betti numbers change when different activation functions are used in deep neural networks. Love et al. (2021) proposed topological convolutional neural networks in deep learning.

In this paper we incorporate topology into learning by minimizing 0D and 1D topological losses as follows. Let $G_1 = (V, w^1), \dots, G_n = (V, w^n)$ be observed networks used for training. Let $P = (V^P, w^P)$ be a network expressing a prior topological knowledge. In brain network analyses, G_k can be a functional brain network of the k th subject obtained from resting-state fMRI, and P can be a template structural brain network obtained through dMRI. Functional brain networks are typically overlaid onto the template structural brain network (Figure 2) (Kang et al. (2017), Lv et al. (2010), Zhu et al. (2014)). Note that the node sets V and V^P may differ, which can happen in the situation where we try to integrate brain networks obtained from different parcellations.

We are interested in learning individual network model $\hat{\Theta}_k$ from the k th training network $G_k = (V, w^k)$ of the k th subject by minimizing

$$(4) \quad \hat{\Theta}_k = \arg \min_{\Theta} \mathcal{L}_F(\Theta, G_k) + \lambda_k \mathcal{L}_{\text{top}}(\Theta, P),$$

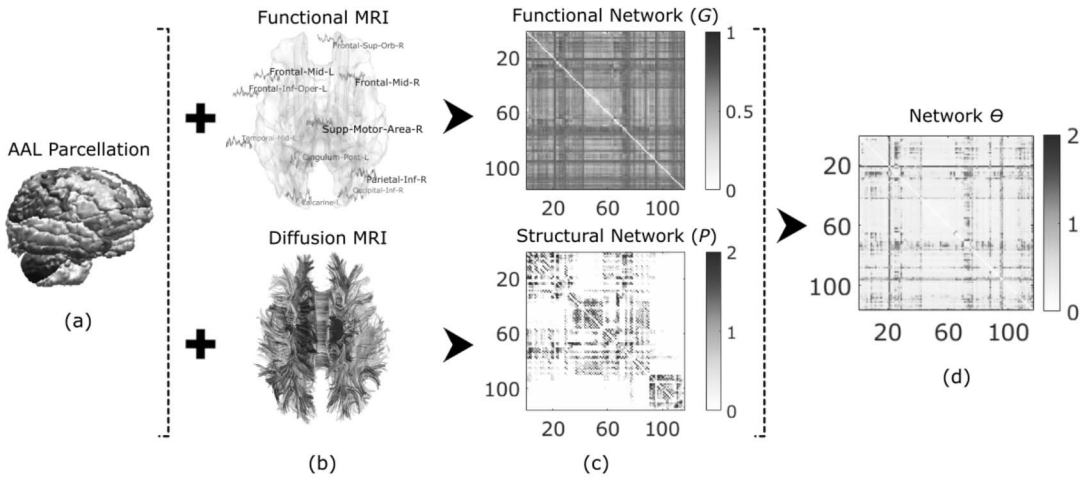


FIG. 2. Schematic illustrating topological learning for brain networks: (a) The automated anatomical labeling (AAL) atlas obtained through structural-MRI is used to partition the human brain into 116 regions forming nodes in brain networks. (b-top) In fMRI, brain activity at each node is measured as a time series of changes associated with the relative blood oxygenation level. (c-top) The functional connectivity between two nodes is given as the correlation between their fMRI time series, which then goes through the metric transform resulting in the functional network G . (b-bottom) The structural connectivity between two brain regions is measured by the number of white matter fiber tracts passing through them using dMRI. (c-bottom) Structural connectivities over all subjects are then normalized and scaled, resulting in the structural network P that serves as the template where statistical analysis can be performed. The structural network P is sparse while the functional network G is densely connected. Since both networks are topologically different, it is difficult to integrate them together in a coherent model. Simply overlaying functional networks on top of the structural network will completely destroy 1D topology (cycles) of the functional networks. (d) The proposed framework learns network Θ that has the topological characteristics of both functional and structural networks.

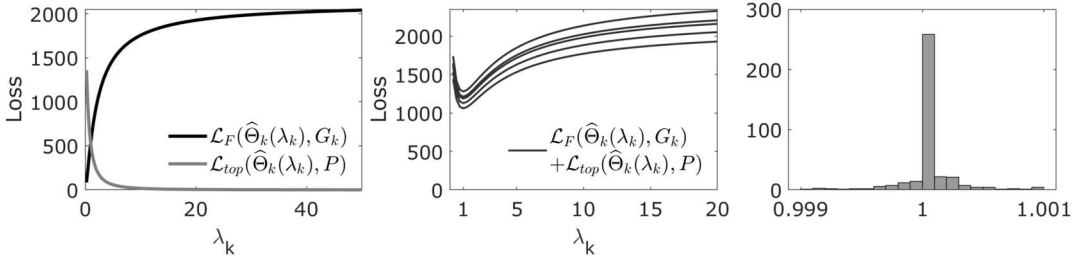


FIG. 3. *Individual-level learning. Left: When $\lambda_k = 0$, the learned network $\hat{\Theta}_k$ is simply the individual network G_k . As λ_k increases, $\hat{\Theta}_k$ is deformed such that the topology of $\hat{\Theta}_k$ is closer to the structural template P . Middle: The sum of losses as a function λ_k for five representative subjects. Optimal λ_k for each individual subject is the one that minimizes the sum of losses. Right: Distribution of optimal λ_k centered around $\lambda = 1.0000 \pm 0.0002$.*

where squared Frobenius loss $\mathcal{L}_F(\Theta, G_k) = \|w^\Theta - w^k\|_F^2$ is the goodness-of-fit term between the model and the individual observation, and parameter λ_k controls the amount of topological information from network P that we are introducing into the model. The larger the value of λ_k , the more we learn toward topology of P . If $\lambda_k = 0$, we no longer learn the topology of P but fit the model only to the individual network G_k . Note that we learn toward the population average since P is the template structural brain network.

Determining optimal λ_k for the k th subject can be done as follows. For each prespecified λ_k , we find optimal $\hat{\Theta}_k$ by minimizing the objective function (4) over all possible Θ . We then determine which λ_k and its corresponding $\hat{\Theta}_k$ give the minimum sum of losses $\mathcal{L}_F + \mathcal{L}_{top}$. Figure 3(left) displays the losses \mathcal{L}_F and \mathcal{L}_{top} as a function of λ_k . Figure 3(middle) displays the sum of losses as a function of λ_k for five representative subjects. Figure 3(right) displays the histogram of the distribution of optimal λ_k based on all subjects. The average optimal λ_k over all subjects is $\lambda_k = 1.0000 \pm 0.0002$, showing highly stable results. Such stable results are not plausible for nontopological loss functions. Similar to the well-known stability result in the persistent homology literature (Cohen-Steiner et al. (2010)), we can algebraically show

$$\mathcal{L}_{top}(\Theta, P) \leq C \|w^\Theta - w^P\|_F^2$$

for some C providing the stability of topological loss. For real data used in this paper, we have the least upper bound of 0.4102 for all subjects.

Although group-level learning is not the focus in this paper, we can also learn a model $\hat{\Theta}$ using multiple training networks such that

$$(5) \quad \hat{\Theta} = \arg \min_{\Theta} \frac{1}{n} \sum_{k=1}^n \mathcal{L}_F(\Theta, G_k) + \lambda \mathcal{L}_{top}(\Theta, P).$$

Figure 4 displays average networks of females and males while Figure 5 displays average networks over all subjects by minimizing the objective function (5) with $\lambda = 0, 1$ and 100. The larger the value of λ , the more we reinforce the average networks with topology of the template structural brain network. Note that statistical significance of network differences between females and males can be determined by using a topological inference developed in our previous work (Chung et al. (2017b), Chung et al. (2019b)).

2.6. Averaging networks of different sizes and topology. Another application of the proposed topological loss is learning the average of networks with different sizes and topology, which is a difficult task using existing methods. Given n networks $G_1 = (V_1, w^1), \dots, G_n = (V_n, w^n)$ with different node sets, we are interested in obtaining its *topological mean*. Since the size and topology of the networks are different, we cannot directly average edge weight matrices w^1, \dots, w^n . Motivated by the Fréchet mean (Le and Kume (2000), Turner et al.

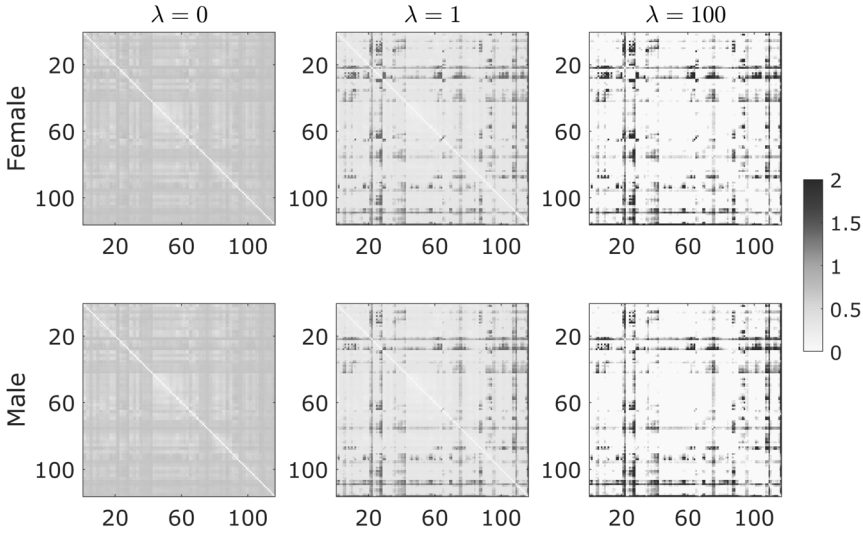


FIG. 4. Group-level networks of female (top row) and male (bottom row) are estimated by minimizing the objective function (5) with different $\lambda = 0, 1$ and 100.

(2014), Zemel and Panaretos (2019)), here we obtain the topological mean $\hat{\Theta}$ by minimizing the sum of 0D and 1D topological losses

$$\hat{\Theta} = \arg \min_{\Theta} \sum_{k=1}^n \mathcal{L}_{\text{top}}(\Theta, G_k) = \arg \min_{\Theta} \sum_{k=1}^n [\mathcal{L}_{0D}(\Theta, G_k) + \mathcal{L}_{1D}(\Theta, G_k)],$$

where $\hat{\Theta}$ is a network viewed as the topological centroid of given n networks. The optimization can be done analytically as follows (Rabin et al. (2011)).

The 0D topological loss \mathcal{L}_{0D} depends on the birth values of networks G_1, \dots, G_n . For networks with the same number of nodes, we have the same m_0 number of birth values. Let $b_{k1} < b_{k2} < \dots < b_{km_0}$ be the birth values of network G_k . Let $\theta_1 < \theta_2 < \dots < \theta_{m_0}$ be the birth values of network Θ . By Theorem 2 the sum of 0D losses is equivalent to

$$\sum_{k=1}^n \mathcal{L}_{0D}(\Theta, G_k) = \sum_{k=1}^n (\theta_1 - b_{k1})^2 + \sum_{k=1}^n (\theta_2 - b_{k2})^2 + \dots + \sum_{k=1}^n (\theta_{m_0} - b_{km_0})^2,$$

which is quadratic so we can find the minimum by setting its derivative equal to zero. The solution is given by $\hat{\theta}_j = \sum_{k=1}^n b_{kj} / n$. Similarly, the sum of 1D losses is equal to the sum of squared differences of death values. Thus, the i th smallest birth (or death) value of the topological mean network $\hat{\Theta}$ is equal to the mean of all the i th smallest birth (or death) values of the given n networks. For networks with different number of nodes, we can match networks through the empirical distribution method described in Section 2.4.

Given all the birth and death values of the topological mean network, we can completely recover its topology. However, the network is only unique in the topological sense but not in a geometric sense. We can have multiple different networks that are geometrically different but with identical topology. For two networks A and B whose edge weights are different, we can have identical birth sets $I_0(A) = I_0(B)$ and identical death sets $I_1(A) = I_1(B)$ so that $\mathcal{L}_{\text{top}}(A, C) = \mathcal{L}_{\text{top}}(B, C)$ for some network C . Such examples can be obtained by permuting node labels or rotating networks geometrically. However, the nonuniqueness may not be disadvantageous in classification and image segmentation. By rotating graphs embedded in 2D images, the number of training samples can be drastically increased, boosting the classification and segmentation performance (Marcos, Volpi and Tuia (2016), Taylor and Nitschke

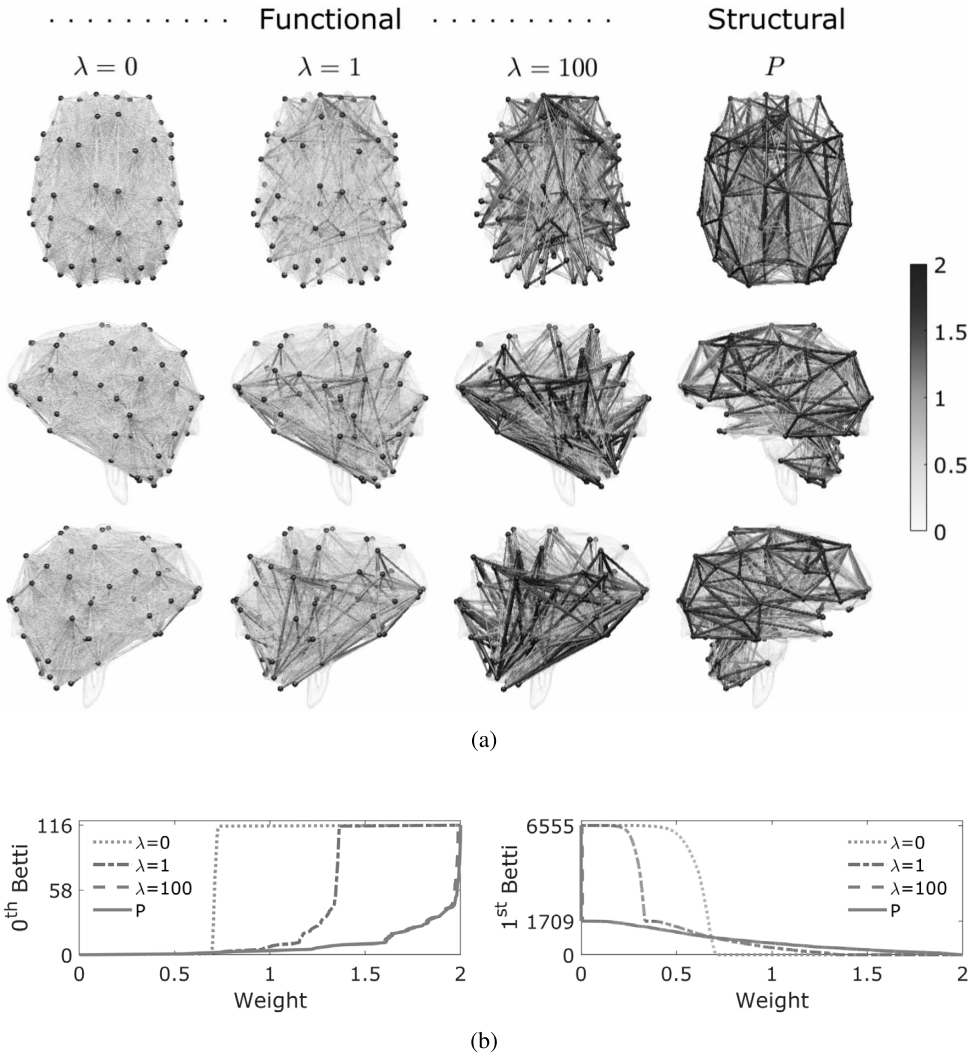


FIG. 5. (a) Group-level networks learned by minimizing the objective function (5) over all subjects with $\lambda = 0, 1$ and 100. Fixed λ is chosen across all the subjects. The template structural network P is shown in the last column. (b) As λ increases, Betti-plots of the group-level network are adjusted toward that of P . β_0 -plot shows that the connected components in the structural network P are gradually born over a wide range of edge weights during the graph filtration. β_1 -plot shows topological sparsity of lack of cycles in the structural network P . While the group-level functional network (when $\lambda = 0$) is densely connected with up to 6555 number of cycles, the structural network is sparsely connected with only 1709 cycles.

(2018)). For brain network application studied in this paper, we are introducing the Frobenius loss that constrains the networks geometrically to avoid this geometric ambiguity. Figure 6 illustrates toy examples of averaging networks of different sizes and topology. Since we can have many differently shaped networks that are topologically equivalent, it is not possible to identify $\hat{\Theta}$ uniquely with the averaged birth and death values. For a Figure 6(top) example, it would be possible for the topological mean network $\hat{\Theta}$ to have the three darker edges extending from one node to the other three remaining nodes.

2.7. Numerical implementation. The topological learning, given in (4), estimates $\Theta = (V^\Theta, w^\Theta)$ iteratively through gradient descent (Saad (1998)). The gradient of the topological loss can be computed efficiently without taking numerical derivatives. In particular, computation of the gradient mainly comprises computing barcodes I_0 and I_1 and finding the optimal

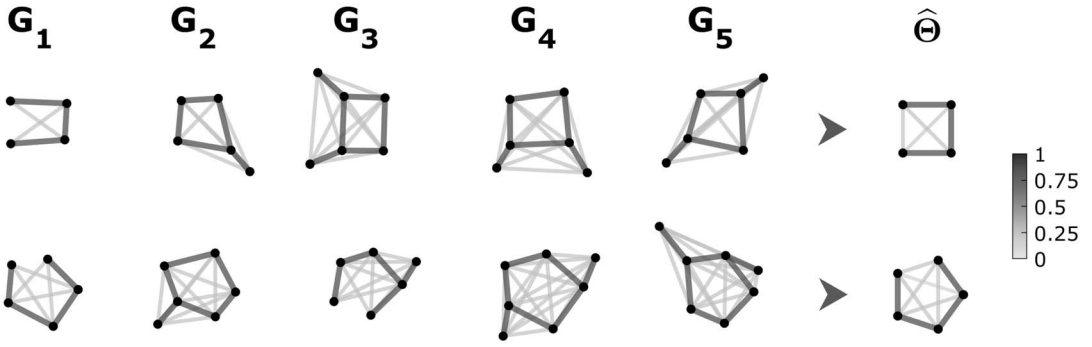


FIG. 6. Examples of averaging networks of different sizes and topology using the empirical distribution method in Section 2.4. The topological mean network $\hat{\Theta}$ (right) is the topological centroid of five networks G_1, \dots, G_5 , showing the average topological pattern. The topological mean network $\hat{\Theta}$ is estimated by minimizing the sum of topological losses $\min_{\Theta} \sum_{k=1}^5 \mathcal{L}_{\text{top}}(\Theta, G_k)$. The topological mean network $\hat{\Theta}$ highlights topological characterization of the five networks. The existing methods will have difficulty averaging networks of different sizes and topology.

matchings through Theorem 2. The gradient of the topological loss $\nabla \mathcal{L}_{\text{top}}(\Theta, P)$ with respect to edge weights $w^{\Theta} = (w_{ij}^{\Theta})$ is given as a gradient matrix whose ij th entry is

$$\frac{\partial \mathcal{L}_{\text{top}}(\Theta, P)}{\partial w_{ij}^{\Theta}} = \begin{cases} 2[w_{ij}^{\Theta} - \tau_0^*(w_{ij}^{\Theta})] & \text{if } w_{ij}^{\Theta} \in I_0(\Theta); \\ 2[w_{ij}^{\Theta} - \tau_1^*(w_{ij}^{\Theta})] & \text{if } w_{ij}^{\Theta} \in I_1(\Theta), \end{cases}$$

since $I_0(\Theta)$ and $I_1(\Theta)$ partition the weight set (Theorem 1). By slightly adjusting the edge weight w_{ij}^{Θ} , we have the slight adjustment of either a birth value in 0D barcode or a death value in 1D barcode, which alters the topology of the network. During the estimation of Θ , we take steps in the direction of negative gradient such that

$$w_{ij}^{\Theta} \leftarrow w_{ij}^{\Theta} - 0.1 \left(2(w_{ij}^{\Theta} - w_{ij}^k) + \lambda \frac{\partial \mathcal{L}_{\text{top}}(\Theta, P)}{\partial w_{ij}^{\Theta}} \right),$$

where 0.1 is the learning rate. As w_{ij}^{Θ} moves closer to its optimal match, the topology of the estimated network Θ gets closer to that of P while the Frobenius norm keeps the estimation Θ close to the observed network G_k .

Finding 0D birth values $I_0(G)$ is equivalent to finding edge weights comprising the maximum spanning tree (MST) of G (Lee et al. (2012)). Once I_0 is computed, I_1 is simply given as the rest of the edge weights (Theorem 1). Then, we can compute the optimal matchings τ_0^* and τ_1^* between Θ and P by matching edge weights in the ascending order. The computational complexity of the topological loss gradient is dominated by the computation of the MST using standard algorithms such as Prim’s and Kruskal’s, which take $O(|E| \log |V|)$ runtime with $|E|$ number of edges and $|V|$ number of vertices.

Many efficient algorithms for Wasserstein distance computation often utilize the geometric structure of data (Sharathkumar and Agarwal (2012)). In particular, Kerber, Morozov and Nigmatov (2017) proposed an approximation algorithm based on k -d trees with the time complexity empirically estimated as $O(n^{1.6})$ for n scatter points in an arbitrary persistence diagram. The estimation is obtained using linear regression on observed running time as a function of n . Translated into the graph filtration setting with $|E|$ number of edges, this is equivalent to $O(|E|^{1.6})$. The approximation algorithm in (Kerber, Morozov and Nigmatov (2017)) is much faster than the Hungarian algorithm with $O(|E|^3)$ but still slower than our exact Wasserstein computation method with $O(|E| \log |V|)$. Note there are $|E| = |V|(|V| - 1)/2$ edges. Our algorithm exploits the geometric structure of the graph filtration resulting

in the one-dimensional representation for persistence diagrams in the form of sorted scalar values. This exploitation enables us to compute the Wasserstein distances exactly at the faster runtime.

3. Validation. We performed two simulation studies to assess the performance of the topological loss as a dissimilarity measure between networks of different topology. Networks of the same size were simulated since many existing methods cannot handle networks of different sizes.

3.1. *Study 1: Random network model with ground truth.* Initial data vector b_i at node i was simulated as independent and identically distributed multivariate normal across n subjects $b_i \sim \mathcal{N}(0, I_n)$ with the identity matrix I_n as the covariance matrix of size $n \times n$. The new data vector x_i at node i was then generated by introducing additional dependency structures to b_i through a mixed-effects model that partitions the covariance matrix of x_i into c blocks forming modular structures (Chung et al. (2019b), Snijders, Spreen and Zwaagstra (1995))

$$\begin{aligned} x_1, \dots, x_a &= b_1 + \mathcal{N}(0, \sigma^2 I_n), \\ x_{a+1}, \dots, x_{2a} &= b_{a+1} + \mathcal{N}(0, \sigma^2 I_n), \\ &\vdots \\ x_{(c-1)a+1}, \dots, x_{ca} &= b_{(c-1)a+1} + \mathcal{N}(0, \sigma^2 I_n), \end{aligned}$$

where a is the number of nodes in each module.

In this simulation, networks with 100 nodes are partitioned into c modules, where c is chosen such that 100 is divisible by c . This choice of c makes the partitioning of each network into modules straightforward. In particular, $c = 2, 5, 10, 20$ number of modules are chosen, and thus there are $a = 50, 20, 10, 5$ nodes in each module, respectively. The simulation is done in small noise ($\sigma = 0.1$) and large noise ($\sigma = 0.5, 1$) settings. Note that it gets more difficult to discriminate between different networks as the variability increases. We compute the Pearson correlation coefficient ρ_{ij}^x between x_i and x_j , which is then translated and scaled as metric $w_{ij}^x = \sqrt{(1 - \rho_{ij}^x)/2}$ (Chung et al. (2019b)). This gives a modular network $\mathcal{X} = (V, w^x)$. Figure 7 shows examples of simulated modular networks.

Based on the statistical model above, we simulated two groups of networks consisting of $n = 7$ subjects in each group. The small sample size was chosen such that exact permutation tests can be done by generating exactly $\binom{14}{7} = 3432$ number of every possible permutation. We employed the exact permutation test for network distances (Chung et al. (2019b)) on the two-sample t -statistic to evaluate the performance of the topological loss \mathcal{L}_{top} relative to several baseline measures. The separate evaluation of \mathcal{L}_{0D} and \mathcal{L}_{1D} helps with understanding the relative performance of the individual 0D and 1D Wasserstein distances in comparison with \mathcal{L}_{top} . Thus, we additionally evaluated the separate performance of \mathcal{L}_{0D} and \mathcal{L}_{1D} . For comparison, we tested the topological loss against Euclidean losses such as \mathcal{L}_1 -, \mathcal{L}_2 - and \mathcal{L}_∞ -norms. We further compared against other topological distances such as bottleneck, Gromov–Hausdorff (GH) and Kolmogorov–Smirnov (KS) distances (Chazal et al. (2009), Chung et al. (2019b), Cohen-Steiner, Edelsbrunner and Harer (2007)). The bottleneck and GH-distance are widely-used baseline distances in persistent homology (Carlsson and Mémoli (2010)) and brain networks (Lee et al. (2012)). KS-distance based on β_0 and β_1 curves is later introduced as an interpretable alternative (Chung et al. (2017a)).

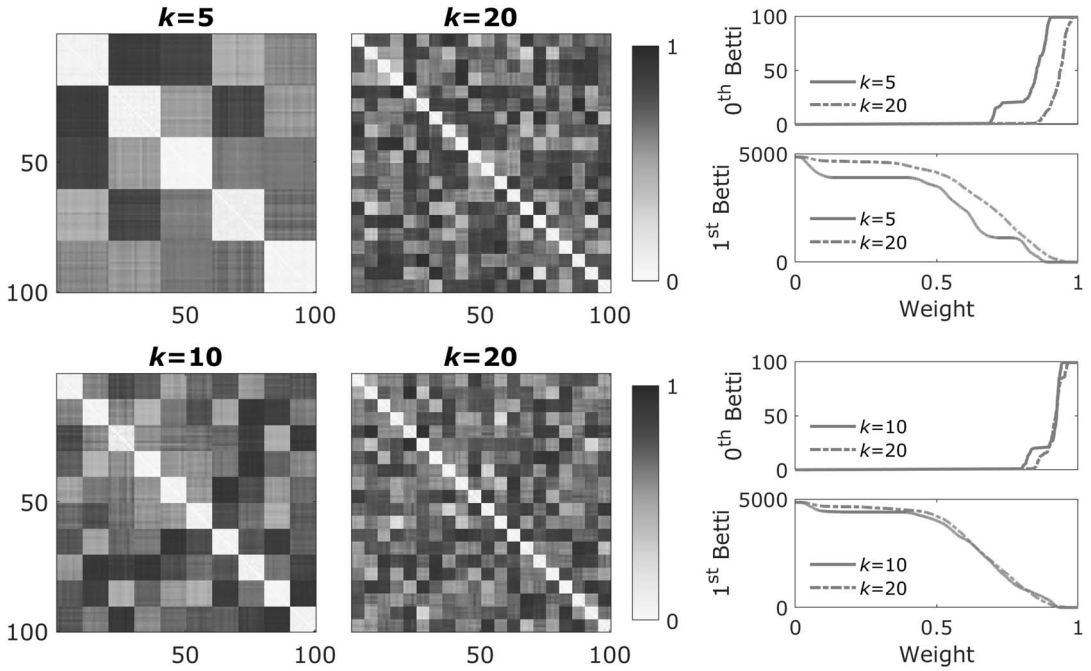


FIG. 7. Study 1 simulation with small noise ($\sigma = 0.1$). The comparison of networks with different topology: $k = 5$ vs. 20 (first row) and 10 vs. 20 (second row). The change of Betti numbers over filtration values shows topological differences. The topological difference in the second row is more subtle compared to the first row.

Network difference. We compared networks with different numbers of modules: 2 vs. 10, 5 vs. 20 and 10 vs. 20. Since the networks had different topological structures, the distances were expected to detect the differences (Figure 7). The simulations were independently performed 50 times, and the performance results were given in terms of the false negative rate computed as the fraction of 50 simulations that gave p -values above 0.05 (Table 1). In general, the topological loss performed relatively well for different noise settings. When the topological difference is obvious ($\sigma = 0.1$), the proposed method performed exceptionally well. However, in the large noise settings ($\sigma = 0.5, 1$), all the distances except the KS-distance did not perform well. Since KS-distances measures the maximum difference over both Betti numbers and filtration values, it is sensitive to topological differences in networks. The sensitivity of KS-distance is advantageous in the high noise settings. On the other hand, \mathcal{L}_{top} mainly penalizes differences in filtration values where topological changes occur and thus is less sensitive than the KS-distance. In addition, \mathcal{L}_{1D} performed substantially better than \mathcal{L}_{0D} in all noise settings. The higher discriminative power of \mathcal{L}_{1D} is expected since there are many more cycles than connected components in networks. In comparison, \mathcal{L}_{top} demonstrated the increase in performance in high noise settings ($\sigma = 0.5, 1$). The improved performance suggests that the combined use of \mathcal{L}_{0D} and \mathcal{L}_{1D} is complementary, and thus \mathcal{L}_{top} is the better choice for differentiating overall network topology.

No network difference. We compared networks of similar topology with the same numbers of modules: 2 vs. 2, 5 vs. 5 and 10 vs. 10. It was expected that the networks were not topologically different, and we should not detect any signal. The simulations were independently performed 50 times, and the performance results were given in terms of the false positive rates computed as the fraction of 50 simulations that gave p -values below 0.05 (Table 1). While most of the baseline distances performed relatively well when there was no network difference, they had the tendency to produce false negatives. The KS-distance did not perform well in all cases and produced false positives, even in the low noise setting ($\sigma = 0.1$).

TABLE 1

Study 1. The performance results are summarized in terms of false negative rates (2 vs. 10, 5 vs. 20, 10 vs. 20) and false positive rates (2 vs. 2, 5 vs. 5, 10 vs. 10). Smaller numbers are better

σ	c	\mathcal{L}_1	\mathcal{L}_2	\mathcal{L}_∞	GH	Bottleneck	KS(β_0)	KS(β_1)	\mathcal{L}_{0D}	\mathcal{L}_{1D}	\mathcal{L}_{top}
0.1	2 vs. 10	0.02	0.00	0.02	0.30	0.40	0.00	0.00	0.70	0.02	0.02
	5 vs. 20	0.06	0.00	0.02	0.20	0.32	0.02	0.00	0.48	0.00	0.00
	10 vs. 20	1.00	0.86	0.34	0.32	0.20	0.24	0.00	0.78	0.08	0.08
	2 vs. 2	0.00	0.00	0.00	0.00	0.00	0.54	0.88	0.00	0.00	0.00
	5 vs. 5	0.00	0.00	0.00	0.00	0.00	0.10	0.42	0.00	0.00	0.00
	10 vs. 10	0.00	0.00	0.00	0.00	0.00	0.02	0.12	0.00	0.00	0.00
0.5	2 vs. 10	0.04	0.02	0.42	0.84	0.60	0.00	0.00	0.66	0.12	0.10
	5 vs. 20	0.16	0.08	0.58	0.82	0.72	0.02	0.00	0.70	0.10	0.08
	10 vs. 20	1.00	0.98	0.80	0.92	0.82	0.06	0.00	0.88	0.68	0.62
	2 vs. 2	0.00	0.00	0.00	0.02	0.00	0.80	0.56	0.00	0.00	0.00
	5 vs. 5	0.00	0.00	0.00	0.02	0.00	0.92	0.58	0.00	0.00	0.00
	10 vs. 10	0.00	0.00	0.00	0.02	0.00	0.98	0.84	0.00	0.00	0.00
1	2 vs. 10	0.12	0.14	0.92	0.90	0.68	0.02	0.00	0.72	0.26	0.24
	5 vs. 20	0.74	0.62	0.92	0.94	0.84	0.06	0.04	0.82	0.58	0.56
	10 vs. 20	1.00	1.00	1.00	0.94	0.96	0.06	0.38	0.92	0.90	0.86
	2 vs. 2	0.00	0.00	0.02	0.02	0.08	0.88	0.40	0.02	0.00	0.00
	5 vs. 5	0.00	0.00	0.00	0.06	0.00	0.92	0.52	0.00	0.00	0.00
	10 vs. 10	0.00	0.00	0.02	0.06	0.00	0.92	0.74	0.00	0.00	0.00

The overly sensitive nature of the KS-distance was responsible for the huge false positives. On the other hand, \mathcal{L}_{top} was significantly more robust than the KS-distance, even in the high noise setting ($\sigma = 1$). There were no significant differences in the performance among \mathcal{L}_{0D} , \mathcal{L}_{1D} and \mathcal{L}_{top} . The almost identical performance suggests that \mathcal{L}_{top} inherits robustness from \mathcal{L}_{0D} and \mathcal{L}_{1D} and is expected to perform relatively well.

3.2. Study 2: Comparison against graph matching algorithms. The aim of this simulation is to evaluate the performance of the proposed topological matching process against existing graph matching algorithms (Cho, Lee and Lee (2010), Gold and Rangarajan (1996), Leordeanu and Hebert (2005), Leordeanu, Hebert and Sukthankar (2009), Zhou and De la Torre (2013)). Given weighted networks $G_1 = (V_1, w^1)$ and $G_2 = (V_2, w^2)$, we need to find mapping τ_{gm} between nodes $i_1, j_1 \in V_1$ and $i_2, j_2 \in V_2$ that best preserves edge attributes between edge weights $w^1_{i_1j_1} \in w^1$ and $w^2_{i_2j_2} \in w^2$. We seek τ_{gm} to maximize the graph matching cost

$$J(\tau_{gm}) = \sum_{w^1_{i_1j_1}, w^2_{i_2j_2}} f(w^1_{i_1j_1}, \tau_{gm}(w^2_{i_2j_2})),$$

where f measures the similarity between edge attributes, and the summation is taken over all possible edge weights. The matching cost $J(\tau_{gm})$ quantifies similarity between networks by taking large values for similar networks and values close to zero for dissimilar networks; hence, $J(\tau_{gm})$ is somewhat the inverse of distance metrics. We compared the proposed topological loss against four graph matching algorithms: graduated assignment (GA) (Gold and Rangarajan (1996)), spectral matching (SM) (Leordeanu and Hebert (2005)), integer projected fixed point method (IPFP) (Leordeanu, Hebert and Sukthankar (2009)) and reweighted random walk matching (RRWM) (Cho, Lee and Lee (2010)). Such graph matching methods are widely used in medical imaging, computer vision and machine learning studies (Cour,

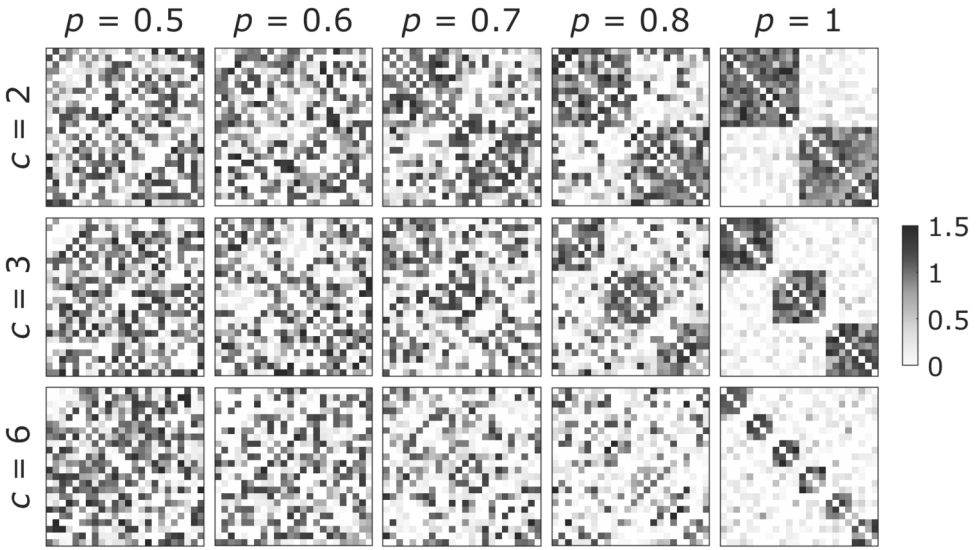


FIG. 8. Study 2 simulation examples. Network modular structures vary as parameter p (probability of connection within modules) and parameter c (the number of modules) change. The modular structure becomes more pronounced as p increases.

Srinivasan and Shi (2006), Tian et al. (2012), Wang et al. (2020), Yu et al. (2018), Zhang et al. (2019b), Zhou and De la Torre (2013)). For all of the baseline methods, we used existing implementations from authors’ repository websites listed in the publication. We also used parameters recommended in the public code for each baseline algorithm *without* modification. Since we are dealing with weighted edges, graph matching algorithms based on binary edge weights (Babai and Luks (1983), Guo and Srivastava (2020), Zavlanos and Pappas (2008)) are excluded in the study.

In study 2, a different random network model from study 1 is used. We simulated a random modular network \mathcal{X} with d number of nodes and c number of modules, where the nodes are evenly distributed among modules. Figure 8 displays modular networks with $d = 24$ nodes and $c = 2, 3, 6$ modules such that we have $d/c = 12, 8, 4$ number of nodes in each module, respectively. Since the time complexity of the aforementioned graph matching baselines can be very demanding (Figure 9), we only considered $d = 12, 18, 24$ and $c = 2, 3, 6$ in this simulation. Each edge connecting two nodes within the same module was then assigned a random weight following a normal distribution $\mathcal{N}(\mu, \sigma^2)$ with probability p and Gaussian

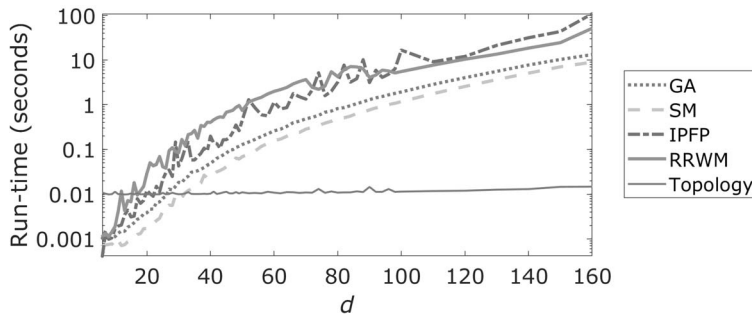


FIG. 9. Study 2 runtime given in the logarithmic scale. The average runtime measures the amount of time each algorithm takes to compute its matching cost between two modular networks of size d starting from edge weights as a given input. The runtime performance of the baseline methods is consistent with Cour, Srinivasan and Shi (2006) for GA and SM and Zhang et al. (2019b) for IPFP and RRWM.

noise $\mathcal{N}(0, \sigma^2)$ with probability $1 - p$. Edge weights connecting nodes between different modules had probability $1 - p$ of being $\mathcal{N}(\mu, \sigma^2)$ and probability p of being $\mathcal{N}(0, \sigma^2)$. With a larger value of within-module probability p , we have a more pronounced modular structure. Any negative edge weights were set to zero. This gives the random network \mathcal{X} that exhibits topological structures of connectedness. Figure 8 illustrates the changes of network modular structure as parameters p and c vary. We used $\mu = 1$ and $\sigma = 0.25$ universally throughout study 2.

Based on the network model above, we simulated two groups of random modular networks $\mathcal{X} = (\mathcal{X}_1, \dots, \mathcal{X}_m)$ and $\mathcal{Y} = (\mathcal{Y}_1, \dots, \mathcal{Y}_n)$. If there is group difference, the topological loss is expected to be relatively small within groups and relatively large between groups. The average topological loss within the groups, given by

$$\bar{\mathcal{L}}_W = \frac{\sum_{i < j} \mathcal{L}_{\text{top}}(\mathcal{X}_i, \mathcal{X}_j) + \sum_{i < j} \mathcal{L}_{\text{top}}(\mathcal{Y}_i, \mathcal{Y}_j)}{\binom{m}{2} + \binom{n}{2}},$$

is expected to be smaller than the average topological loss between the groups, given by

$$\bar{\mathcal{L}}_B = \frac{\sum_{i=1}^m \sum_{j=1}^n \mathcal{L}_{\text{top}}(\mathcal{X}_i, \mathcal{Y}_j)}{mn}.$$

We measure the disparity between groups as the ratio $\phi_{\mathcal{L}}$

$$\phi_{\mathcal{L}} = \bar{\mathcal{L}}_B / \bar{\mathcal{L}}_W.$$

If $\phi_{\mathcal{L}}$ is large, the groups differ significantly in network topology. On the other hand, if $\phi_{\mathcal{L}}$ is small, it is likely that there is no group difference. Similarly, we define the ratio statistic for graph matching cost J as

$$\phi_J = \bar{J}_W / \bar{J}_B,$$

where \bar{J}_W is the average graph matching cost within groups, and \bar{J}_B is the average graph matching cost between groups. Since the distributions of the ratios $\phi_{\mathcal{L}}$ and ϕ_J are unknown, the permutation test is used to determine the empirical distributions. Figure 10 displays the empirical distribution of $\phi_{\mathcal{L}}$. By comparing the observed ratio $\phi_{\mathcal{L}}$ to the empirical distribution, we can determine the statistical significance of testing the group difference. However, when the sample size is large, existing matching algorithms are too slow for the permutation test. To this end, we adapted a scalable online computation strategy as follows.

Given two groups of networks, topological loss or graph matching cost for every pair of networks needs to be computed only once, which can then be arranged into a matrix whose rows and columns represent networks. The ij th entry is the loss between two networks corresponding to row i and column j (Figure 11). Once we obtain such a matrix, the permutation

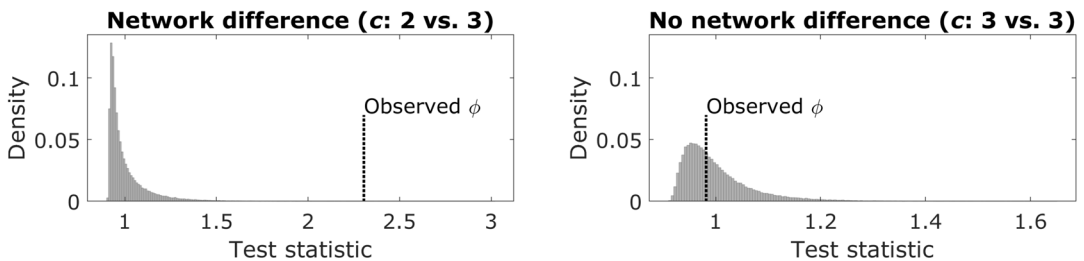


FIG. 10. The empirical distribution of the ratio statistic $\phi_{\mathcal{L}}$ is generated by the permutation on two groups each consisting of ten modular networks. Here, we test if there is group difference in networks with parameters $c = 2$ vs. 3 (left) and 3 vs. 3 (right). As expected, the test based on the topological loss rejects the null hypothesis when there is group difference (left) while it does not reject when there is no difference (right).

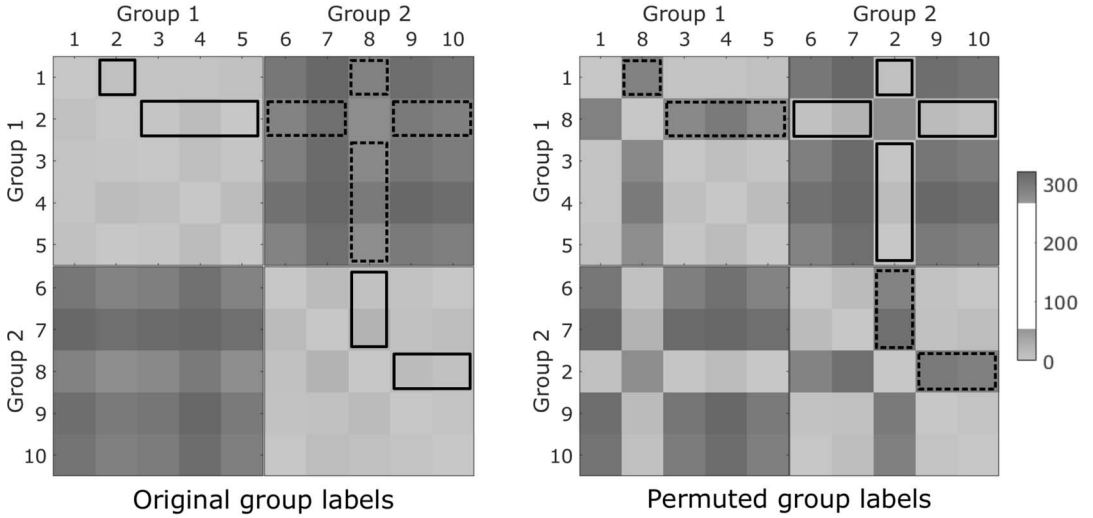


FIG. 11. Two groups each consisting of five modular networks are simulated with parameters $c = 2$ vs. 3. Left: The ij th entry represents the loss \mathcal{L}_{top} between networks i and j . The main diagonal consists of zeros since the topological loss between two identical networks is zero. Right: A transposition between the second network in Group 1 and the eighth network in Group 2. We do not need to recompute all the pairwise losses again but just rearrange the losses in the solid lines and dashed lines. Thus, we simply need to find out how the rearrangement changes the ratio statistic in an iterative manner. This enables us to efficiently perform the permutation test in an iterative fashion. We compute δ in equation (6) by subtracting the sum of entries within the solid lines from the sum of entries within the dashed lines.

process is equivalent to rearranging rows and columns based on permuted group labels. There are $\frac{1}{2} \binom{m+n}{m}$ total number of permutations excluding the symmetry. Computing the ratio over a permutation requires resummation over all such losses, which is time consuming. Instead, we performed the transposition procedure of swapping only one network per group and setting up iteration of how the ratio changes over the transposition.

We transpose k th and l th networks between the groups as

$$\begin{aligned}\pi_{kl}(\mathcal{X}) &= (\mathcal{X}_1, \dots, \mathcal{X}_{k-1}, \mathcal{Y}_l, \mathcal{X}_{k+1}, \dots, \mathcal{X}_m), \\ \pi_{kl}(\mathcal{Y}) &= (\mathcal{Y}_1, \dots, \mathcal{Y}_{l-1}, \mathcal{X}_k, \mathcal{Y}_{l+1}, \dots, \mathcal{Y}_n).\end{aligned}$$

Over transposition π_{kl} , the ratio statistic is changed from $\phi_L(\mathcal{X}, \mathcal{Y})$ to $\phi_L(\pi_{kl}(\mathcal{X}), \pi_{kl}(\mathcal{Y}))$, which involves the following functions:

$$\begin{aligned}v(\mathcal{X}, \mathcal{Y}) &= \sum_{i < j} \mathcal{L}_{\text{top}}(\mathcal{X}_i, \mathcal{X}_j) + \sum_{i < j} \mathcal{L}_{\text{top}}(\mathcal{Y}_i, \mathcal{Y}_j), \\ \omega(\mathcal{X}, \mathcal{Y}) &= \sum_{i=1}^m \sum_{j=1}^n \mathcal{L}_{\text{top}}(\mathcal{X}_i, \mathcal{Y}_j),\end{aligned}$$

where v is the total sum of within-group losses, and ω is the total sum of between-group losses. Then, we determine how v and ω change over the transposition π_{kl} . As \mathcal{X}_k and \mathcal{Y}_l are swapped, the function v is updated over the transposition π_{kl} as (Figure 11)

$$v(\pi_{kl}(\mathcal{X}), \pi_{kl}(\mathcal{Y})) = v(\mathcal{X}, \mathcal{Y}) + \delta(\mathcal{X}, \mathcal{Y})$$

with

$$(6) \quad \delta(\mathcal{X}, \mathcal{Y}) = \sum_{i \neq k} \mathcal{L}_{\text{top}}(\mathcal{Y}_l, \mathcal{X}_i) - \sum_{i \neq k} \mathcal{L}_{\text{top}}(\mathcal{X}_k, \mathcal{X}_i) + \sum_{i \neq l} \mathcal{L}_{\text{top}}(\mathcal{X}_k, \mathcal{Y}_i) - \sum_{i \neq l} \mathcal{L}_{\text{top}}(\mathcal{Y}_l, \mathcal{Y}_i).$$

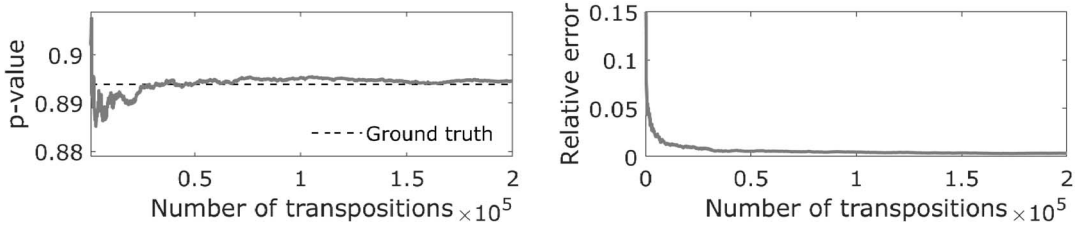


FIG. 12. The transition test is used to determine the statistical significance of two groups each consisting of ten simulated networks. To further speed up the convergence rate, a random permutation is intermixed for every consecutive sequence of 500 transpositions. Left: The plot showing the convergence of p -value over 50,000 transpositions. For comparison, ground truth p -value is computed from the exact permutation test by enumerating every possible permutation exactly once. Right: The plot shows the average relative error against the ground truth across 100 independent simulations.

Similarly, function ω is updated iteratively over the transposition π_{kl} as

$$\omega(\pi_{kl}(\mathcal{X}), \pi_{kl}(\mathcal{Y})) = \omega(\mathcal{X}, \mathcal{Y}) - \delta(\mathcal{X}, \mathcal{Y}).$$

The ratio statistic over the transposition is then computed as

$$\phi_{\mathcal{L}}(\pi_{kl}(\mathcal{X}), \pi_{kl}(\mathcal{Y})) = \frac{\omega(\pi_{kl}(\mathcal{X}), \pi_{kl}(\mathcal{Y}))}{v(\pi_{kl}(\mathcal{X}), \pi_{kl}(\mathcal{Y}))} \times \frac{\binom{m}{2} + \binom{n}{2}}{mn}.$$

For each transposition we store information about function values v and ω and update them sequentially. Each transposition requires manipulating $2(m + n - 2)$ terms, as opposed to $\binom{m+n}{2}$ total number of terms over a random permutation. More transpositions than the number of permutations can be generated within the same amount of time, which speeds up the convergence (Chung et al. (2019c)). To further accelerate the rate of convergence and avoid possible bias, we introduce a full permutation to the sequence of 500 consecutive transpositions. Figure 12 illustrates the convergence of transposition procedure.

In each simulation we generated two groups each with ten random modular networks. We then sequentially computed 200,000 random transpositions while interjecting a random permutation for every 500 transpositions and obtained the p -value. This indicated the convergence of p -value within two decimal places (within 0.01) in average. The simulations were independently performed 50 times, and the average p -value was reported.

Network difference. We compared two groups of networks generated by parameters $c = 2$ vs. 3, 2 vs. 6 and 3 vs. 6 each with $d = 12, 18, 24$ nodes and $p = 0.6, 0.8$ probability of connection within modules. Since each group exhibited a different modular structure, topological loss and graph matching costs were expected to detect the group difference. Table 2 summarizes the performance results. Networks with $d = 12$ nodes might be too small to extract distinct features used in each algorithm. Thus, all graph matching costs performed poorly while the topological loss performed reasonably well. When the number of nodes increases, all methods show overall performance improvement. In all settings the topological loss significantly outperformed other graph matching algorithms.

No network difference. We compared networks generated with parameters $c = 2$ vs. 2, 3 vs. 3 and 6 vs. 6 each with $d = 12, 18, 24$ nodes and $p = 0.6, 0.8$ probability of connection within modules. Since it was expected that there was no topological difference between networks generated using the same values for parameters c, d and p , the topological loss and graph matching costs should not be able to detect the group difference. The performance result is summarized in Table 3. All the methods performed relatively well when there was

TABLE 2

Study 2 on network differences. The performance results are summarized as the average p -values for various parameter settings of d (number of nodes), c (number of modules) and p (within-module probability)

d	c	p	GA	SM	RRWM	IPFP	\mathcal{L}_{top}
12 vs. 12	2 vs. 3	0.6	0.45 ± 0.27	0.48 ± 0.30	0.28 ± 0.31	0.34 ± 0.28	0.08 ± 0.16
		0.8	0.26 ± 0.24	0.30 ± 0.28	0.06 ± 0.12	0.28 ± 0.28	0.01 ± 0.03
	2 vs. 6	0.6	0.06 ± 0.10	0.17 ± 0.20	0.04 ± 0.13	0.23 ± 0.28	0.00 ± 0.00
		0.8	0.00 ± 0.01	0.01 ± 0.03	0.00 ± 0.00	0.02 ± 0.04	0.00 ± 0.00
	3 vs. 6	0.6	0.40 ± 0.29	0.35 ± 0.28	0.24 ± 0.26	0.35 ± 0.28	0.06 ± 0.13
		0.8	0.21 ± 0.23	0.28 ± 0.27	0.08 ± 0.14	0.26 ± 0.25	0.00 ± 0.01
18 vs. 18	2 vs. 3	0.6	0.25 ± 0.23	0.41 ± 0.26	0.26 ± 0.24	0.42 ± 0.28	0.01 ± 0.02
		0.8	0.12 ± 0.17	0.19 ± 0.22	0.00 ± 0.00	0.04 ± 0.05	0.00 ± 0.00
	2 vs. 6	0.6	0.02 ± 0.05	0.07 ± 0.17	0.00 ± 0.00	0.14 ± 0.20	0.00 ± 0.00
		0.8	0.00 ± 0.00				
	3 vs. 6	0.6	0.28 ± 0.24	0.37 ± 0.31	0.21 ± 0.24	0.37 ± 0.30	0.01 ± 0.01
		0.8	0.15 ± 0.22	0.13 ± 0.14	0.00 ± 0.01	0.16 ± 0.18	0.00 ± 0.00
24 vs. 24	2 vs. 3	0.6	0.23 ± 0.25	0.30 ± 0.26	0.14 ± 0.20	0.31 ± 0.28	0.00 ± 0.01
		0.8	0.06 ± 0.11	0.12 ± 0.19	0.00 ± 0.00	0.01 ± 0.05	0.00 ± 0.00
	2 vs. 6	0.6	0.00 ± 0.01	0.03 ± 0.06	0.00 ± 0.00	0.09 ± 0.13	0.00 ± 0.00
		0.8	0.00 ± 0.00				
	3 vs. 6	0.6	0.24 ± 0.26	0.29 ± 0.28	0.10 ± 0.13	0.37 ± 0.26	0.00 ± 0.00
		0.8	0.07 ± 0.12	0.13 ± 0.19	0.00 ± 0.01	0.12 ± 0.19	0.00 ± 0.00

TABLE 3

Study 2 on no network difference. The performance results are summarized as average p -values for various parameter settings of d (number of nodes), c (number of modules) and p (within-module probability)

d	c	p	GA	SM	RRWM	IPFP	\mathcal{L}_{top}
12 vs. 12	2 vs. 2	0.6	0.49 ± 0.27	0.46 ± 0.30	0.51 ± 0.30	0.47 ± 0.28	0.53 ± 0.29
		0.8	0.45 ± 0.25	0.47 ± 0.31	0.56 ± 0.29	0.47 ± 0.30	0.50 ± 0.30
	3 vs. 3	0.6	0.45 ± 0.32	0.44 ± 0.26	0.47 ± 0.27	0.51 ± 0.30	0.46 ± 0.31
		0.8	0.54 ± 0.31	0.51 ± 0.27	0.51 ± 0.29	0.52 ± 0.29	0.51 ± 0.30
	6 vs. 6	0.6	0.57 ± 0.30	0.51 ± 0.28	0.56 ± 0.29	0.45 ± 0.26	0.58 ± 0.29
		0.8	0.55 ± 0.29	0.48 ± 0.26	0.52 ± 0.27	0.54 ± 0.30	0.49 ± 0.27
18 vs. 18	2 vs. 2	0.6	0.48 ± 0.26	0.49 ± 0.32	0.54 ± 0.29	0.47 ± 0.30	0.54 ± 0.31
		0.8	0.52 ± 0.28	0.50 ± 0.28	0.46 ± 0.30	0.52 ± 0.25	0.50 ± 0.26
	3 vs. 3	0.6	0.49 ± 0.28	0.58 ± 0.31	0.43 ± 0.28	0.51 ± 0.27	0.53 ± 0.30
		0.8	0.46 ± 0.30	0.51 ± 0.27	0.52 ± 0.33	0.45 ± 0.29	0.53 ± 0.27
	6 vs. 6	0.6	0.53 ± 0.28	0.48 ± 0.30	0.51 ± 0.30	0.45 ± 0.29	0.44 ± 0.33
		0.8	0.54 ± 0.27	0.52 ± 0.30	0.48 ± 0.26	0.52 ± 0.31	0.43 ± 0.30
24 vs. 24	2 vs. 2	0.6	0.52 ± 0.28	0.49 ± 0.30	0.50 ± 0.30	0.48 ± 0.28	0.55 ± 0.26
		0.8	0.53 ± 0.27	0.56 ± 0.30	0.51 ± 0.30	0.56 ± 0.32	0.52 ± 0.30
	3 vs. 3	0.6	0.48 ± 0.29	0.54 ± 0.27	0.49 ± 0.26	0.49 ± 0.30	0.52 ± 0.30
		0.8	0.55 ± 0.29	0.49 ± 0.27	0.52 ± 0.28	0.49 ± 0.30	0.47 ± 0.26
	6 vs. 6	0.6	0.47 ± 0.30	0.45 ± 0.31	0.51 ± 0.29	0.56 ± 0.28	0.49 ± 0.29
		0.8	0.51 ± 0.30	0.47 ± 0.28	0.54 ± 0.28	0.56 ± 0.31	0.51 ± 0.31

no group difference. The baseline graph matching methods have low sensitivity to topological differences. They were unable to detect the network differences when the topological differences were subtle.

While graph matching algorithms can be applied to dense networks, a small increment in the number of possible connections usually results in a combinatorial explosion of the amount of data to fit (Zhou and De la Torre (2013)). Thus, most high-order graph matching methods are often limited to sparse networks like binary trees. They are not practical in dense functional brain networks with a far large number of cycles. On the other hand, the proposed topological loss is able to detect such subtle topological differences without the added computational burden.

4. Application. In standard brain network modeling framework, the whole brain is parcellated into d disjoint regions, where d is usually a few hundreds (Arslan et al. (2018), Desikan et al. (2006), Eickhoff, Yeo and Genon (2018), Fan et al. (2016), Fornito, Zalesky and Bullmore (2010, 2016), Glasser et al. (2016), Gong et al. (2009), Hagmann et al. (2007), Schaefer et al. (2017), Shattuck et al. (2008), Tzourio-Mazoyer et al. (2002), Zalesky et al. (2010)). Subsequently, functional or structural information is overlaid on top of the parcellation to obtain $d \times d$ connectivity matrices that measure the strength of connectivity between brain regions (Figure 2). These disjoint brain regions form nodes in the brain network. Connectivity between brain regions that defines edges in the brain network is usually determined by the type of imaging modality (Ombao et al. (2016)). Structural connectivity is obtained through diffusion MRI (dMRI), which traces the white matter fibers connecting brain regions. The strength of structural connectivity between brain regions is determined by the number of fibers passing through them (Fornito, Zalesky and Bullmore (2016)). The structural brain network is expected to exhibit sparse topology without many loops or cycles (Figure 2) (Chung et al. (2011), Gong et al. (2009), Zhang et al. (2018)). On the other hand, functional connectivity obtained from the resting-state functional MRI (fMRI) is often computed as the Pearson correlation coefficient between brain regions (Bryant et al. (2017), Shappell et al. (2019)). While structural connectivity provides information whether the brain regions are physically connected through white matter fibers, functional connectivity exhibits connections between two regions without the direct neuroanatomical connections through additional intermediate connections (Honey et al. (2007, 2009)). Thus, resting-state functional brain networks are often very dense with thousands of cycles. Both structural and functional brain networks provide topologically different information. Existing graph theory based brain network analyses have shown that there is some common topological profile that is conserved for both structural and functional brain networks (Bullmore and Sporns (2009)). However, due to the difficulty of integrating both networks in a coherent statistical framework, not much research has been done on integrating such networks at the localized connection level. Many previous studies focus on comparing summary graph theory features across different networks (Bullmore and Sporns (2009), Ginestet et al. (2011), Karas et al. (2019)). Although there are few studies that focus on fusing networks derived from both modalities probabilistically, such methods can easily destroy the aforementioned topological difference of the networks (Kang et al. (2017), Xue et al. (2015)). This motivates the development of a model for multimodal networks that can integrate networks of different topology at the localized connection level.

4.1. Dataset and preprocessing. Dataset studied in this paper is the resting-state fMRI of 412 subjects collected as part of the Human Connectome Project (HCP) twin study (Van Essen et al. (2012), Van Essen et al. (2013)). The fMRI were collected over 14 minutes and 33 seconds using a gradient-echo-planar imaging (EPI) sequence with multiband factor 8, repetition time (TR) 720 ms, time echo (TE) 33.1 ms, flip angle 52° , 104×90 (RO \times PE) matrix

size, 72 slices, 2 mm isotropic voxels, and 1200 time points. Subjects without fMRI or full 1200 time points were excluded. During scanning, participants were at rest with eyes open with relaxed fixation on a projected bright crosshair on a dark background (Van Essen et al. (2013)). The standard minimal preprocessing pipelines (Glasser et al. (2013)) were applied on the fMRI scans, including spatial distortion removal (Andersson, Skare and Ashburner (2003), Jovicich et al. (2006)), motion correction (Jenkinson and Smith (2001), Jenkinson et al. (2002)), bias field reduction (Glasser and Essen (2011)), registration to the structural MNI template and data masking using the brain mask obtained from FreeSurfer (Glasser et al. (2013)). This resulted in the resting-state functional time series with $91 \times 109 \times 91$ 2-mm isotropic voxels at 1200 time points. The subject ranged from 22 to 36 years in age with average age 29.24 ± 3.39 years. There are 172 males and 240 females. Among them, there are 131 monozygotic (MZ) twin pairs and 75 same-sex dizygotic (DZ) twin pairs.

Subsequently, we employed the automated anatomical labeling (AAL) template to parcellate the brain volume into 116 nonoverlapping anatomical regions (Tzourio-Mazoyer et al. (2002)) (Figure 2). We averaged fMRI across voxels within each brain parcellation, resulting in 116 average fMRI time series with 1200 time points for each subject. Previous studies reported that head movement produces spatial artifacts in functional connectivity (Caballero-Gaudes and Reynolds (2017), Power et al. (2012), Satterthwaite et al. (2012), Van Dijk, Sabuncu and Buckner (2012)). Thus, we scrubbed the data with significant head motion using the framewise displacement (FD) from the three translational displacements and three rotational displacements at each time point to measure the head movement from one volume to the next (Huang et al. (2020), Power et al. (2012), Van Dijk, Sabuncu and Buckner (2012)). We excluded 12 subjects having excessive head movement, resulting in fMRI data of 400 subjects (168 males and 232 females). Among the remaining 400 subjects, there are $p = 124$ MZ twin pairs and $q = 70$ same-sex DZ twin pairs. The first 20 time points were removed from all subjects to avoid artifacts in the fMRI data, leaving 1180 time points per subject (Diedrichsen and Shadmehr (2005), Shah et al. (2016)).

For dMRI we use the template structural brain network P (Figure 2) published in previous studies (Chung et al. (2019c), Songdechakruiwut, Shen and Chung (2021)). Preprocessing pipeline for P reported in those studies is as follows. The white matter fiber orientation information was extracted by multishell, multitissue constrained spherical deconvolution from different tissue types, such as white matter and gray matter (Callaghan, Eccles and Xia (1988), Jeurissen et al. (2014)). The fiber orientation distribution functions were estimated and apparent fiber densities were exploited to produce the reliable white and gray matter volume maps (Christiaens et al. (2015), Jeurissen et al. (2014)). Subsequently, multiple random seeds were selected in each voxel to generate about 10 million initial streamlines per subject with the maximum fiber tract length at 250 mm and FA larger than 0.06 using MRtrix3 (Tournier et al. (2012), Xie et al. (2018)). The spherical-deconvolution informed filtering of tractograms (SIFT2) technique making use of complete streamlines was subsequently applied to generate more biologically accurate brain connectivity, which resulted in about one million tracts per subject (Smith et al. (2015)). Nonlinear diffeomorphic registration between subject images to the template was performed using ANTS (Avants et al. (2008, 2011)). AAL was used to parcellate the brain into 116 regions (Tzourio-Mazoyer et al. (2002)). The subject-level connectivity matrices were constructed by counting the number of tracts connecting between brain regions. The structural brain network P that serves as the template, where all the functional networks are aligned, was obtained by computing the one sample t -statistic map over all the subjects and then rescaling t -statistics between 0 to 2 using the hyperbolic tangent function \tanh before adding 1.

4.2. *Learning individual networks.* For subject k we have resting-state fMRI time series $x = (x_1, x_2, \dots, x_{1180})$ for region i and $y = (y_1, y_2, \dots, y_{1180})$ for region j with 1180 time points. Correlation ρ_{ij}^k between regions i and j is computed using the Pearson correlation between x and y . This gives the correlation matrix $C_k = (\rho_{ij}^k)$, which is used as the baseline against our proposed method. We then translate and scale the correlation as $w_{ij}^k = \sqrt{(1 - \rho_{ij}^k)/2}$, which is a metric (Chung et al. (2019b)). The subject-level functional brain network is given by $G_k = (V, w^k)$.

We apply the topological learning to estimate the subject-level network $\Theta_k(\lambda_k)$ by minimizing the objective function (4) using the individual network G_k and the structural network P

$$\widehat{\Theta}_k(\lambda_k) = \arg \min_{\Theta} \mathcal{L}_F(\Theta, G_k) + \lambda_k \mathcal{L}_{\text{top}}(\Theta, P).$$

Θ is initialized to G_k . λ_k was found to be 1.0000 ± 0.0002 , and thus we globally used $\lambda = 1.0000$ (Figure 3).

4.3. *Heritability in twins.* We employ our method to explore which regions of brain networks are genetically heritable. In particular, we determine if the estimated network $\widehat{\Theta}_k$ is genetically heritable in twins. At each edge, let (a_{1l}, a_{2l}) be the l th twin pair in MZ-twin and (b_{1l}, b_{2l}) be the l th twin pair in DZ-twin. MZ-twin and DZ-twin pairs are then represented as

$$a = \begin{pmatrix} a_{11} & \cdots & a_{1p} \\ a_{21} & \cdots & a_{2p} \end{pmatrix}, \quad b = \begin{pmatrix} b_{11} & \cdots & b_{1q} \\ b_{21} & \cdots & b_{2q} \end{pmatrix}.$$

Let $a_r = (a_{r1}, a_{r2}, \dots, a_{rp})$ and $b_r = (b_{r1}, b_{r2}, \dots, b_{rq})$ be the r th rows. Then, MZ-correlation is computed as the Pearson correlation $\gamma^{MZ}(a_1, a_2)$ between a_1 and a_2 . Similarly, DZ-correlation $\gamma^{DZ}(b_1, b_2)$ is computed. In the well established ACE genetic model, the heritability index (HI) h , which determines the amount of variation caused by genetic factors in population, is estimated using Falconer’s formula (Falconer and Mackay (1995))

$$h(a, b) = 2(\gamma^{MZ} - \gamma^{DZ}).$$

Since the order of the twins is interchangeable, we can *transpose* the l th twin pair in MZ-twin as

$$\begin{aligned} \pi_l(a_1) &= (a_{11}, \dots, a_{1,l-1}, a_{2l}, a_{1,l+1}, \dots, a_{1p}), \\ \pi_l(a_2) &= (a_{21}, \dots, a_{2,l-1}, a_{1l}, a_{2,l+1}, \dots, a_{2p}) \end{aligned}$$

and obtain another MZ-correlation $\gamma^{MZ}(\pi_l(a_1), \pi_l(a_2))$. Likewise, we can obtain many different correlation values for DZ-twin. To this end, we perform a sequence of random transpositions iteratively to estimate the twin correlations γ^{MZ} and γ^{DZ} sequentially, similar to the transposition test used in the simulation study 2, as follows.

Over the transposition π_l , the MZ-correlation is changed from $\gamma^{MZ}(a_1, a_2)$ to $\gamma^{MZ}(\pi_l(a_1), \pi_l(a_2))$, which involves the following functions:

$$\begin{aligned} v(a_r) &= \sum_{j=1}^p a_{rj}, \\ \omega(a_r, a_s) &= \sum_{j=1}^p (a_{rj} - v(a_r)/p)(a_{sj} - v(a_s)/p). \end{aligned}$$

The functions v and ω are updated iteratively over the transposition π_l as

$$v(\pi_l(a_r)) = v(a_r) - a_{rl} + a_{sl},$$

$$\omega(\pi_l(a_r), \pi_l(a_s)) = \omega(a_r, a_s) + (a_{rl} - a_{sl})^2/p - (a_{rl} - a_{sl})(\mu(a_r) - \mu(a_s))/p.$$

Then, MZ-correlation after the transposition is calculated as

$$\gamma^{MZ}(\pi_l(a_1), \pi_l(a_2)) = \frac{\omega(\pi_l(a_1), \pi_l(a_2))}{\sqrt{\omega(\pi_l(a_1), \pi_l(a_1))\omega(\pi_l(a_2), \pi_l(a_2))}}.$$

The time complexity for computing correlation iteratively is 33 operations per transposition, which is significantly more efficient than that of direct correlation computation per permutation. In our numerical implementation we sequentially perform random transpositions $\pi_{l_1}, \pi_{l_2}, \dots, \pi_{l_J}$ resulting in J different twin correlations. Let

$$\kappa_1 = \pi_{l_1}, \quad \kappa_2 = \pi_{l_2} \circ \pi_{l_1}, \quad \dots, \quad \kappa_J = \pi_{l_J} \circ \dots \circ \pi_{l_2} \circ \pi_{l_1}$$

be the sequence of transpositions. The average MZ-correlation $\bar{\gamma}_J^{MZ}$ is then given by

$$\bar{\gamma}_J^{MZ} = \frac{1}{J} \sum_{j=1}^J \gamma^{MZ}(\kappa_j(a_1), \kappa_j(a_2)),$$

which is iteratively updated as

$$\bar{\gamma}_J^{MZ} = \frac{J-1}{J} \bar{\gamma}_{J-1}^{MZ} + \frac{1}{J} \gamma^{MZ}(\kappa_J(a_1), \kappa_J(a_2)).$$

The average correlation $\bar{\gamma}_J^{MZ}$ converges to the true underlying twin correlation γ^{MZ} for sufficiently large J . Similarly, DZ-correlation γ^{DZ} is estimated.

4.4. Results. Using the transposition method, we randomly transposed twins and updated the correlations for 50,000 times. This process was repeated 100 times, and the total $50,000 \times 100$ correlations were used to estimate the underlying MZ- and DZ-correlations. At each edge the standard deviation of the average correlations from 100 results was smaller than 0.01 indicating the convergence of the estimate within two decimal places in average.

We computed HI-maps using the original correlation matrices C_k and the proposed topologically learned networks $\hat{\Theta}_k$. Figure 13 displays most heritable connections with 100% heritability, indicating that the topologically learned networks $\hat{\Theta}_k$ show more connections than the original Pearson correlation matrices C_k . Table 4 shows that left superior parietal lobule and left amygdala connection has the strongest heritability among many other connections using the topologically learned networks. Since the networks $\hat{\Theta}_k$ inherited sparse topology from the template structural brain network P (Figure 5), short-lived cycles in the functional networks were expected to be removed resulting in the increased statistical sensitivity to subtle genetic signals. There are significant connection overlaps between the standard method and the topology-based approach, but our approach detects more connections with higher HI. Figure 14 displays heritable connections above HI value 0.85. If correlation thresholds are altered to values below 0.85, more connections will appear resulting in more overlaps.

5. Discussion. We present a new topological loss for graphs that provides the optimal matching and alignment at the edge level. Unlike many existing graph matching algorithms (Babai and Luks (1983), Guo and Srivastava (2020), Tian et al. (2012), Wang et al. (2020), Yu et al. (2018), Zhang et al. (2019b), Zhou and De la Torre (2013)) that provide matching costs without explicit identification of how edges are matched to each other, the proposed method identifies the edge-to-edge correspondence explicitly using the birth-death decomposition.

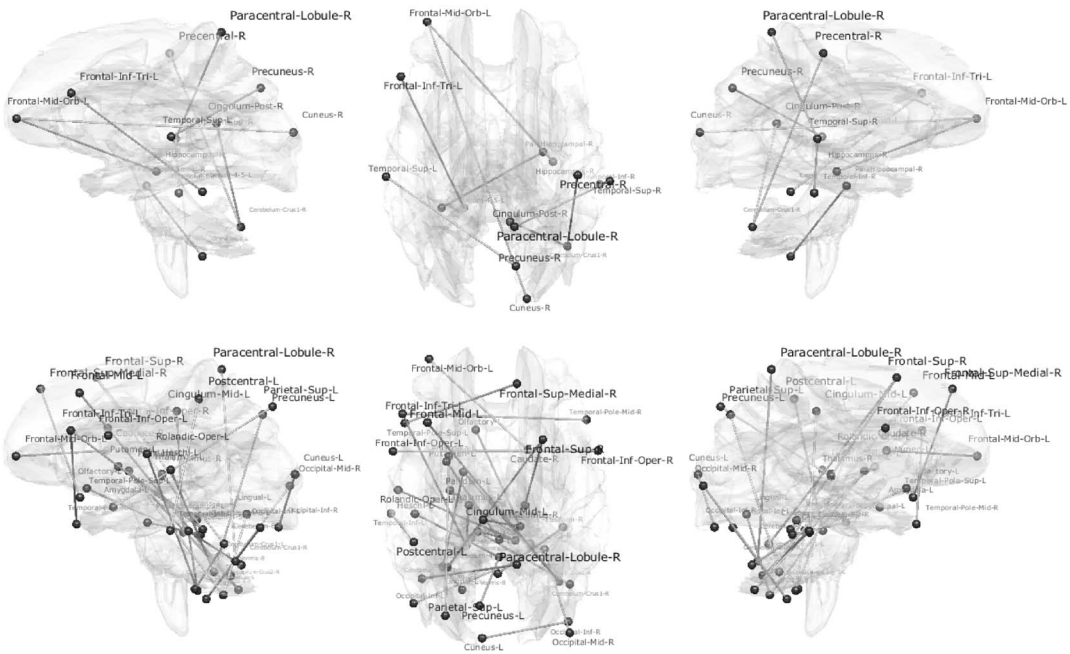


FIG. 13. *Most heritable connections above $HI \geq 1$ are shown using the Pearson correlation baseline (top row) and our topologically learned network approach (bottom row).*

Such explicit mapping enables us to develop the subsequent topological learning framework that can integrate networks of different sizes and topology. Due to the wide availability of various network data including social networks, computer networks and artificial networks (such as convolutional neural networks), our method can be easily adapted for other network applications where matching of whole networks or subnetworks is needed.

The limitation of the topological loss is the inability to discriminate geometrically different networks that have identical topology. We can obtain topologically identical networks by mirror reflection. Since the human brain is asymmetric across hemispheres (Toga and Thompson (2003)), the ability to discriminate such networks is critical. In our application we introduced the Frobenius loss to geometrically constrain brain networks. We provided one possible approach for combining the topological and geometrical losses together. Hopefully, this paper serves as the springboard for more refined models in the future.

TABLE 4

Top ten most heritable connections with $HI \geq 1$ using the proposed topologically learned networks

Most heritable connections

Left superior parietal lobule—Left amygdala
 Left lobule VIIIB of cerebellar hemisphere—Left globus pallidus
 Left lobule III of cerebellar hemisphere—Right crus I of cerebellar hemisphere
 Left—Right opercular part of inferior frontal gyrus
 Left lobule IV, V of cerebellar hemisphere—Left thalamus
 Left lobule IX of cerebellar hemisphere—Left lobule VI of cerebellar hemisphere
 Right thalamus—Right superior frontal gyrus, dorsolateral
 Left middle frontal gyrus, orbital part—Right caudate nucleus
 Right crus II of cerebellar hemisphere—Left globus pallidus
 Lobule VIII of vermis—Right fusiform gyrus

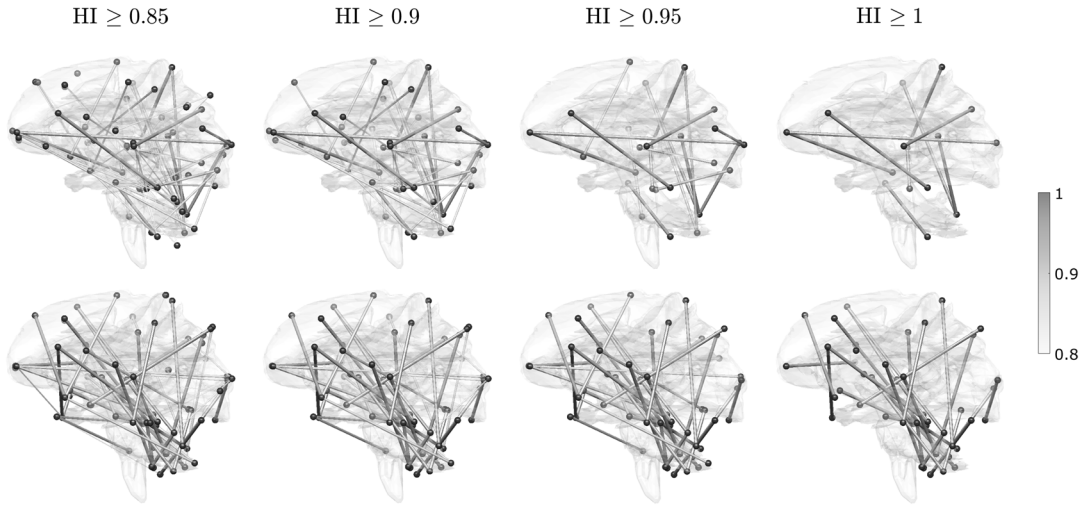


FIG. 14. *HI-maps for the Pearson correlation baseline (top row) and our topologically learned network approach (bottom row) are thresholded at different $HI \geq 0.85, 0.9, 0.95$ and 1 .*

Among many different learning tasks, the proposed method is illustrated with averaging and regression. Our method can be used to average networks of different sizes and topology, which is challenging using prior methods. Our method is further used to set up the optimization-based regression models at the subject and group levels. We believe the proposed method can be easily adapted to other types of network learning tasks. For example, it is well known that k -means clustering does not perform well against more geometry-based clustering methods, such as spectral clustering (Kriegel, Kröger and Zimek (2009), Ng, Jordan and Weiss (2002)). A new clustering method that utilizes meaningful network topology is expected to outperform k -means and spectral clustering methods. Recently, it was shown that topological clustering using our proposed framework demonstrates very strong performance for clustering measured functional brain networks used to evaluate biomarkers of the neural basis of consciousness (Songdechakraiwut et al. (2022b)). We believe that the demonstrated effectiveness and computational elegance of our topological framework will have a high impact on the analysis of brain networks.

Existing network predictive models typically employ various forms of regressions, such as linear models and logistic regressions, that incorporate the accumulated effect of network features into prediction scores (Arslan et al. (2018), Eickhoff et al. (2016), Goodfellow, Bengio and Courville (2016), Huang et al. (2021), Kong et al. (2019), Rottschy et al. (2012), Zhang et al. (2019a)). While the use of these methods may be reasonable to discover the underlying network features and their combinations for prediction, the development of new methods using the proposed topological loss may provide additional insights into network analyses. This is left as a future study.

The proposed method is applied to multimodal brain networks in the twin brain imaging study. We determine the extent to which brain networks are genetically heritable by using the heritability index, which is twice the difference between MZ- and DZ-twin correlations. Due to the possible swapping of twin pairing, twin correlations are not unique. This has been considered as a main weakness of the widely-used ACE model in genetics. We remedy the problem by computing a sufficiently large number of permutations over twin labels through the transposition test. This enables us to perform the network analysis at the edge level even when network shapes and topologies are different. We believe that the transposition test would be useful in various resampling problems beyond twin correlations. This is left as a future study.

Acknowledgments. We thank Hernando Ombao of King Abdullah University of Science and Technology (KAUST) for discussion on brain network modeling. We thank Gary Shiu of University of Wisconsin–Madison for discussion on stability theorem. We thank Li Shen of University of Pennsylvania for providing the template structural brain network used in our twin brain imaging study. We thank Shih-Gu Huang of National University of Singapore for providing fMRI preprocessing support.

Funding. This study is funded by NIH Grants R01 EB022856, EB02875, and NSF Grant MDS-2010778.

REFERENCES

- ADLER, R. J., AGAMI, S. and PRANAV, P. (2017). Modeling and replicating statistical topology and evidence for CMB nonhomogeneity. *Proc. Natl. Acad. Sci. USA* **114** 11878–11883. MR3725115 <https://doi.org/10.1073/pnas.1706885114>
- ADLER, R. J., BOBROWSKI, O., BORMAN, M. S., SUBAG, E. and WEINBERGER, S. (2010). Persistent homology for random fields and complexes. In *Borrowing Strength: Theory Powering Applications—A Festschrift for Lawrence D. Brown. Inst. Math. Stat. (IMS) Collect.* **6** 124–143. IMS, Beachwood, OH. MR2798515
- ANDERSSON, J. L., SKARE, S. and ASHBURNER, J. (2003). How to correct susceptibility distortions in spin-echo echo-planar images: Application to diffusion tensor imaging. *NeuroImage* **20** 870–888.
- ARSLAN, S., K TENA, S. I., MAKROPOULOS, A., ROBINSON, E. C., RUECKERT, D. and PARISOT, S. (2018). Human brain mapping: A systematic comparison of parcellation methods for the human cerebral cortex. *NeuroImage* **170** 5–30. <https://doi.org/10.1016/j.neuroimage.2017.04.014>
- AVANTS, B. B., EPSTEIN, C. L., GROSSMAN, M. and GEE, J. C. (2008). Symmetric diffeomorphic image registration with cross-correlation: Evaluating automated labeling of elderly and neurodegenerative brain. *Med. Image Anal.* **12** 26–41. <https://doi.org/10.1016/j.media.2007.06.004>
- AVANTS, B. B., TUSTISON, N. J., SONG, G., COOK, P. A., KLEIN, A. and GEE, J. C. (2011). A reproducible evaluation of ANTs similarity metric performance in brain image registration. *NeuroImage* **54** 2033–2044.
- BABAI, L. and LUKS, E. M. (1983). Canonical labeling of graphs. In *Proceedings of the Fifteenth Annual ACM Symposium on Theory of Computing* 171–183.
- BENDICH, P., MARRON, J. S., MILLER, E., PIELOCH, A. and SKWERER, S. (2016). Persistent homology analysis of brain artery trees. *Ann. Appl. Stat.* **10** 198–218. MR3480493 <https://doi.org/10.1214/15-AOAS886>
- BLOKLAND, G. A. M., MCMAHON, K. L., THOMPSON, P. M., MARTIN, N. G., DE ZUBICARAY, G. I. and WRIGHT, M. J. (2011). Heritability of working memory brain activation. *J. Neurosci.* **31** 10882–10890.
- BONNEEL, N., RABIN, J., PEYRÉ, G. and PFISTER, H. (2015). Sliced and Radon Wasserstein barycenters of measures. *J. Math. Imaging Vision* **51** 22–45. MR3300482 <https://doi.org/10.1007/s10851-014-0506-3>
- BRYANT, C., ZHU, H., AHN, M. and IBRAHIM, J. (2017). LCN: A random graph mixture model for community detection in functional brain networks. *Stat. Interface* **10** 369–378. MR3608546 <https://doi.org/10.4310/SII.2017.v10.n3.a1>
- BULLMORE, E. and SPORNS, O. (2009). Complex brain networks: Graph theoretical analysis of structural and functional systems. *Nat. Rev. Neurosci.* **10** 186–198.
- CABALLERO-GAUDES, C. and REYNOLDS, R. C. (2017). Methods for cleaning the BOLD fMRI signal. *NeuroImage* **154** 128–149. <https://doi.org/10.1016/j.neuroimage.2016.12.018>
- CALLAGHAN, P. T., ECCLES, C. D. and XIA, Y. (1988). NMR microscopy of dynamic displacements: k-space and q-space imaging. *J. Phys. E, Sci. Instrum.* **21** 820.
- CARLSSON, G. (2009). Topology and data. *Bull. Amer. Math. Soc. (N.S.)* **46** 255–308. MR2476414 <https://doi.org/10.1090/S0273-0979-09-01249-X>
- CARLSSON, G. and MÉMOLI, F. (2010). Characterization, stability and convergence of hierarchical clustering methods. *J. Mach. Learn. Res.* **11** 1425–1470. MR2645457
- CARRIERE, M., CUTURI, M. and OUDOT, S. (2017). Sliced Wasserstein kernel for persistence diagrams. In *International Conference on Machine Learning* 664–673. PMLR.
- CHAZAL, F., COHEN-STEINER, D., GUIBAS, L. J., MÉMOLI, F. and OUDOT, S. Y. (2009). Gromov–Hausdorff stable signatures for shapes using persistence. In *Computer Graphics Forum* **28** 1393–1403. Wiley Online Library.
- CHAZAL, F., GUIBAS, L. J., OUDOT, S. Y. and SKRABA, P. (2013). Persistence-based clustering in Riemannian manifolds. *J. ACM* **60** Art. 41, 38 pp. MR3144911 <https://doi.org/10.1145/2535927>
- CHEN, C., NI, X., BAI, Q. and WANG, Y. (2019). A topological regularizer for classifiers via persistent homology. In *The 22nd International Conference on Artificial Intelligence and Statistics* 2573–2582.

- CHIANG, M. C., MCMAHON, K. L., DE ZUBICARAY, G. I., MARTIN, N. G., HICKIE, I., TOGA, A. W., WRIGHT, M. J. and THOMPSON, P. M. (2011). Genetics of white matter development: A DTI study of 705 twins and their siblings aged 12 to 29. *NeuroImage* **54** 2308–2317.
- CHO, M., LEE, J. and LEE, K. M. (2010). Reweighted random walks for graph matching. In *European Conference on Computer Vision* 492–505. Springer, Berlin.
- CHRISTIAENS, D., REISERT, M., DHOLLANDER, T., SUNAERT, S., SUETENS, P. and MAES, F. (2015). Global tractography of multi-shell diffusion-weighted imaging data using a multi-tissue model. *NeuroImage* **123** 89–101. <https://doi.org/10.1016/j.neuroimage.2015.08.008>
- CHUNG, M. K. and OMBAO, H. (2021). Lattice paths for persistent diagrams. In *Interpretability of Machine Intelligence in Medical Image Computing, and Topological Data Analysis and Its Applications for Medical Data. LNCS* **12929** 77–86.
- CHUNG, M. K., ADLURU, N., DALTON, K. M., ALEXANDER, A. L. and DAVIDSON, R. J. (2011). Scalable brain network construction on white matter fibers. *Proc. SPIE Int. Soc. Opt. Eng.* **7962** 1403–1408. <https://doi.org/10.1117/12.874245>
- CHUNG, M. K., HUANG, S.-G., GRITSENKO, A., SHEN, L. and LEE, H. (2019a). Statistical inference on the number of cycles in brain networks. In *2019 IEEE 16th International Symposium on Biomedical Imaging (ISBI 2019)* 113–116. IEEE, New York.
- CHUNG, M. K., LEE, H., DICHRISTOFANO, A., OMBAO, H. and SOLO, V. (2019b). Exact topological inference of the resting-state brain networks in twins. *Netw. Neurosci.* **3** 674–694.
- CHUNG, M. K., XIE, L., HUANG, S.-G., WANG, Y., YAN, J. and SHEN, L. (2019c). Rapid acceleration of the permutation test via transpositions. In *International Workshop on Connectomics in NeuroImaging* 42–53. Springer, Berlin.
- CHUNG, M. K., LEE, H., SOLO, V., DAVIDSON, R. J., POLLAK, S. D. (2017a). Topological distances between brain networks. In *Connectomics in Neuroimaging: First International Workshop* **10511** 161–170. Springer, Berlin. https://doi.org/10.1007/978-3-319-67159-8_19
- CHUNG, M. K., VILLALTA-GIL, V., LEE, H., RATHOUZ, P. J., LAHEY, B. B. and ZALD, D. H. (2017b). Exact topological inference for paired brain networks via persistent homology. In *International Conference on Information Processing in Medical Imaging* 299–310. Springer, Berlin.
- CLOUGH, J. R., OKSUZ, I., BYRNE, N., SCHNABEL, J. A. and KING, A. P. (2019). Explicit topological priors for deep-learning based image segmentation using persistent homology. In *International Conference on Information Processing in Medical Imaging* 16–28. Springer, Berlin.
- COHEN-STEINER, D., EDELSBRUNNER, H. and HARER, J. (2007). Stability of persistence diagrams. *Discrete Comput. Geom.* **37** 103–120. MR2279866 <https://doi.org/10.1007/s00454-006-1276-5>
- COHEN-STEINER, D., EDELSBRUNNER, H., HARER, J. and MILEYKO, Y. (2010). Lipschitz functions have L_p -stable persistence. *Found. Comput. Math.* **10** 127–139. MR2594441 <https://doi.org/10.1007/s10208-010-9060-6>
- COUR, T., SRINIVASAN, P. and SHI, J. (2006). Balanced graph matching. *Adv. Neural Inf. Process. Syst.* **19** 313–320.
- CRAWFORD, L., MONOD, A., CHEN, A. X., MUKHERJEE, S. and RABADÁN, R. (2020). Predicting clinical outcomes in glioblastoma: An application of topological and functional data analysis. *J. Amer. Statist. Assoc.* **115** 1139–1150. MR4143455 <https://doi.org/10.1080/01621459.2019.1671198>
- DESHPANDE, I., ZHANG, Z. and SCHWING, A. G. (2018). Generative modeling using the sliced Wasserstein distance. In *Proceedings of the IEEE Conference on Computer Vision and Pattern Recognition* 3483–3491.
- DESIKAN, R. S., SÉGONNE, F., FISCHL, B., QUINN, B. T., DICKERSON, B. C., BLACKER, D., BUCKNER, R. L., DALE, A. M., MAGUIRE, R. P. et al. (2006). An automated labeling system for subdividing the human cerebral cortex on MRI scans into gyral based regions of interest. *NeuroImage* **31** 968–980.
- DIEDRICHSSEN, J. and SHADMEHR, R. (2005). Detecting and adjusting for artifacts in fMRI time series data. *NeuroImage* **27** 624–634.
- EDELSBRUNNER, H. and HARER, J. (2008). Persistent homology—A survey. In *Surveys on Discrete and Computational Geometry. Contemp. Math.* **453** 257–282. Amer. Math. Soc., Providence, RI. MR2405684 <https://doi.org/10.1090/conm/453/08802>
- EDELSBRUNNER, H., LETSCHER, D. and ZOMORODIAN, A. (2000). Topological persistence and simplification. In *41st Annual Symposium on Foundations of Computer Science (Redondo Beach, CA, 2000)* 454–463. IEEE Comput. Soc. Press, Los Alamitos, CA. MR1931842 <https://doi.org/10.1109/SFCS.2000.892133>
- EDMONDS, J. and KARP, R. M. (1972). Theoretical improvements in algorithmic efficiency for network flow problems. *J. ACM* **19** 248–264.
- EICKHOFF, S. B., NICHOLS, T. E., LAIRD, A. R., HOFFSTAEDTER, F., AMUNTS, K., FOX, P. T., BZDOK, D. and EICKHOFF, C. R. (2016). Behavior, sensitivity, and power of activation likelihood estimation characterized by massive empirical simulation. *NeuroImage* **137** 70–85. <https://doi.org/10.1016/j.neuroimage.2016.04.072>

- EICKHOFF, S. B., YEO, B. T. T. and GENON, S. (2018). Imaging-based parcellations of the human brain. *Nat. Rev. Neurosci.* **19** 672–686.
- FALCONER, D. and MACKAY, T. (1995). *Introduction to Quantitative Genetics*, 4th ed. Longman, Harlow.
- FAN, L., LI, H., ZHUO, J., ZHANG, Y., WANG, J., CHEN, L., YANG, Z., CHU, C., XIE, S. et al. (2016). The human brainnetome atlas: A new brain atlas based on connectional architecture. *Cereb. Cortex* **26** 3508–3526.
- FORNITO, A., ZALESKY, A. and BULLMORE, E. T. (2010). Network scaling effects in graph analytic studies of human resting-state fMRI data. *Front. Syst. Neurosci.* **4** 1–16.
- FORNITO, A., ZALESKY, A. and BULLMORE, E. (2016). *Fundamentals of Brain Network Analysis*. Academic Press, New York.
- GHRIST, R. (2008). Barcodes: The persistent topology of data. *Bull. Amer. Math. Soc. (N.S.)* **45** 61–75. MR2358377 <https://doi.org/10.1090/S0273-0979-07-01191-3>
- GINESTET, C. E., NICHOLS, T. E., BULLMORE, E. T. and SIMMONS, A. (2011). Brain network analysis: Separating cost from topology using cost-integration. *PLoS ONE* **6** e21570. <https://doi.org/10.1371/journal.pone.0021570>
- GLAHN, D. C., WINKLER, A. M., KOCHUNOV, P., ALMASY, L., DUGGIRALA, R., CARLESS, M. A., CURRAN, J. C., OLVERA, R. L., LAIRD, A. R. et al. (2010). Genetic control over the resting brain. *Proc. Natl. Acad. Sci. USA* **107** 1223–1228.
- GLASSER, M. F. and ESSEN, D. C. V. (2011). Mapping human cortical areas in vivo based on myelin content as revealed by T1- and T2-weighted MRI. *J. Neurosci.* **31** 11597–11616. <https://doi.org/10.1523/JNEUROSCI.2180-11.2011>
- GLASSER, M. F., SMITH, S. M., MARCUS, D. S., ANDERSSON, J. L. R., AUERBACH, E. J., BEHRENS, T. E. J., COALSON, T. S., HARMS, M. P., JENKINSON, M. et al. (2016). The human connectome project’s neuroimaging approach. *Nat. Neurosci.* **19** 1175.
- GLASSER, M. F., SOTIROPOULOS, S. N., WILSON, J. A., COALSON, T. S., FISCHL, B., ANDERSSON, J. L., XU, J., JBABDI, S., WEBSTER, M. et al. (2013). The minimal preprocessing pipelines for the Human Connectome Project. *NeuroImage* **80** 105–124.
- GOLD, S. and RANGARAJAN, A. (1996). A graduated assignment algorithm for graph matching. *IEEE Trans. Pattern Anal. Mach. Intell.* **18** 377–388.
- GONG, G., HE, Y., CONCHA, L., LEBEL, C., GROSS, D. W., EVANS, A. C. and BEAULIEU, C. (2009). Mapping anatomical connectivity patterns of human cerebral cortex using in vivo diffusion tensor imaging tractography. *Cereb. Cortex* **19** 524–536.
- GOODFELLOW, I., BENGIO, Y. and COURVILLE, A. (2016). *Deep Learning. Adaptive Computation and Machine Learning*. MIT Press, Cambridge, MA. MR3617773
- GRITSENKO, A., LINDQUIST, M. A. and CHUNG, M. K. (2020). Twin classification in resting-state brain connectivity. In *IEEE International Symposium on Biomedical Imaging (ISBI)*. Available at [arXiv:1807.00244](https://arxiv.org/abs/1807.00244).
- GUO, X. and SRIVASTAVA, A. (2020). Representations, metrics and statistics for shape analysis of elastic graphs. In *Proceedings of the IEEE/CVF Conference on Computer Vision and Pattern Recognition Workshops* 832–833.
- HAGMANN, P., KURANT, M., GIGANDET, X., THIRAN, P., WEDEEN, V. J., MEULI, R. and THIRAN, J.-P. (2007). Mapping human whole-brain structural networks with diffusion MRI. *PLoS ONE* **2** e597. <https://doi.org/10.1371/journal.pone.0000597>
- HONEY, C. J., KÖTTER, R., BREAKSPEAR, M. and SPORNS, O. (2007). Network structure of cerebral cortex shapes functional connectivity on multiple time scales. *Proc. Natl. Acad. Sci. USA* **104** 10240–10245.
- HONEY, C. J., SPORNS, O., CAMMOUN, L., GIGANDET, X., THIRAN, J.-P., MEULI, R. and HAGMANN, P. (2009). Predicting human resting-state functional connectivity from structural connectivity. *Proc. Natl. Acad. Sci. USA* **106** 2035–2040.
- HU, X., LI, F., SAMARAS, D. and CHEN, C. (2019). Topology-preserving deep image segmentation. In *Advances in Neural Information Processing Systems* 5657–5668.
- HUANG, S. G., CHUNG, M. K., QIU, A. and INITIATIVE, A. D. N. (2021). Revisiting convolutional neural network on graphs with polynomial approximations of Laplace–Beltrami spectral filtering. *Neural Comput. Appl.* **33** 13693–13704.
- HUANG, S. G., SAMDIN, S. T., TING, C. M., OMBAO, H. and CHUNG, M. K. (2020). Statistical model for dynamically-changing correlation matrices with application to brain connectivity. *J. Neurosci. Methods* **331** 108480.
- JENKINSON, M. and SMITH, S. (2001). A global optimisation method for robust affine registration of brain images. *Med. Image Anal.* **5** 143–156.
- JENKINSON, M., BANNISTER, P., BRADY, M. and SMITH, S. (2002). Improved optimization for the robust and accurate linear registration and motion correction of brain images. *NeuroImage* **17** 825–841.

- JEURISSEN, B., TOURNIER, J.-D., DHOLLANDER, T., CONNELLY, A. and SIJBERS, J. (2014). Multi-tissue constrained spherical deconvolution for improved analysis of multi-shell diffusion MRI data. *NeuroImage* **103** 411–426. <https://doi.org/10.1016/j.neuroimage.2014.07.061>
- JOVICICH, J., CZANNER, S., GREVE, D., HALEY, E., VAN DER KOUWE, A., GOLLUB, R., KENNEDY, D., SCHMITT, F., BROWN, G. et al. (2006). Reliability in multi-site structural MRI studies: Effects of gradient non-linearity correction on phantom and human data. *NeuroImage* **30** 436–443.
- KANG, H., OMBAO, H., FONNESBECK, C., DING, Z. and MORGAN, V. L. (2017). A Bayesian double fusion model for resting-state brain connectivity using joint functional and structural data. *Brain Connect.* **7** 219–227. <https://doi.org/10.1089/brain.2016.0447>
- KARAS, M., BRZYSKI, D., DZEMIDZIC, M., GOŃI, J., KAREKEN, D. A., RANDOLPH, T. W. and HAREZLAK, J. (2019). Brain connectivity-informed regularization methods for regression. *Stat. Biosci.* **11** 47–90. <https://doi.org/10.1007/s12561-017-9208-x>
- KARRAS, T., AILA, T., LAINE, S. and LEHTINEN, J. (2018). Progressive growing of GANs for improved quality, stability, and variation. In *International Conference on Learning Representations*.
- KERBER, M., MOROZOV, D. and NIGMETOV, A. (2017). Geometry helps to compare persistence diagrams. *ACM J. Exp. Algorithmics* **22** Art. 1.4, 20 pp. MR3707737 <https://doi.org/10.1145/3064175>
- KOLOURI, S., NADJARI, K., SIMSEKLI, U., BADEAU, R. and ROHDE, G. (2019). Generalized sliced Wasserstein distances. In *Advances in Neural Information Processing Systems* 261–272.
- KOLOURI, S., PARK, S. R., THORPE, M., SLEPCEV, D. and ROHDE, G. K. (2017). Optimal mass transport: Signal processing and machine-learning applications. *IEEE Signal Process. Mag.* **34** 43–59.
- KONG, R., GAO, J., XU, Y., PAN, Y., WANG, J. and LIU, J. (2019). Classification of autism spectrum disorder by combining brain connectivity and deep neural network classifier. *Neurocomputing* **324** 63–68.
- KRIEGL, H.-P., KRÖGER, P. and ZIMEK, A. (2009). Clustering high-dimensional data: A survey on subspace clustering, pattern-based clustering, and correlation clustering. *ACM Trans. Knowl. Discov. Data* **3** 1–58.
- LE, H. and KUME, A. (2000). The Fréchet mean shape and the shape of the means. *Adv. in Appl. Probab.* **32** 101–113. MR1765168 <https://doi.org/10.1239/aap/1013540025>
- LEE, H., KANG, H., CHUNG, M. K., KIM, B.-N. and LEE, D. S. (2012). Persistent brain network homology from the perspective of dendrogram. *IEEE Trans. Med. Imag.* **31** 2267–2277.
- LEORDEANU, M. and HEBERT, M. (2005). A spectral technique for correspondence problems using pairwise constraints. In *Tenth IEEE International Conference on Computer Vision (ICCV'05), Volume 1* 2 1482–1489. IEEE, New York.
- LEORDEANU, M., HEBERT, M. and SUKTHANKAR, R. (2009). An integer projected fixed point method for graph matching and map inference. In *Advances in Neural Information Processing Systems* 1114–1122.
- LIUTKUS, A., SIMSEKLI, U., MAJEWSKI, S., DURMUS, A. and STÖTER, F.-R. (2019). Sliced-Wasserstein flows: Nonparametric generative modeling via optimal transport and diffusions. In *International Conference on Machine Learning* 4104–4113.
- LOVE, E. R., FILIPPENKO, B., MAROULAS, V. and CARLSSON, G. (2021). Topological deep learning. Preprint. Available at arXiv:2101.05778.
- LY, J., GUO, L., HU, X., ZHANG, T., LI, K., ZHANG, D., YANG, J. and LIU, T. (2010). Fiber-centered analysis of brain connectivities using DTI and resting state fMRI data. In *International Conference on Medical Image Computing and Computer-Assisted Intervention (MICCAI)* 143–150. Springer, Berlin.
- MARCHESE, A. and MAROULAS, V. (2018). Signal classification with a point process distance on the space of persistence diagrams. *Adv. Data Anal. Classif.* **12** 657–682. MR3854422 <https://doi.org/10.1007/s11634-017-0294-x>
- MARCOS, D., VOLPI, M. and TUIA, D. (2016). Learning rotation invariant convolutional filters for texture classification. In *2016 23rd International Conference on Pattern Recognition (ICPR) 2012–2017*. IEEE, New York.
- MAROULAS, V., NASRIN, F. and OBALLE, C. (2020). A Bayesian framework for persistent homology. *SIAM J. Math. Data Sci.* **2** 48–74. MR4060450 <https://doi.org/10.1137/19M1268719>
- MCKAY, D. R., KNOWLES, E. E. M., WINKLER, A. A. M., SPROOTEN, E., KOCHUNOV, P., OLVERA, R. L., CURRAN, J. E., KENT JR., J. W., CARLESS, M. A. et al. (2014). Influence of age, sex and genetic factors on the human brain. *Brain Imaging Behav.* **8** 143–152.
- NAITZAT, G., ZHITNIKOV, A. and LIM, L.-H. (2020). Topology of deep neural networks. *J. Mach. Learn. Res.* **21** Paper No. 184, 40 pp. MR4209470
- NG, A. Y., JORDAN, M. I. and WEISS, Y. (2002). On spectral clustering: Analysis and an algorithm. In *Advances in Neural Information Processing Systems* 849–856.
- OMBAO, H., LINDQUIST, M., THOMPSON, W. and ASTON, J., eds. (2016). *Handbook of Neuroimaging Data Analysis. Chapman & Hall/CRC Handbooks of Modern Statistical Methods*. CRC Press, Boca Raton, FL. MR3618824
- PATRANGENARU, V., BUBENIK, P., PAIGE, R. L. and OSBORNE, D. (2019). Challenges in topological object data analysis. *Sankhya A* **81** 244–271. MR3982197 <https://doi.org/10.1007/s13171-018-0137-7>

- POWER, J. D., BARNES, K. A., SNYDER, A. Z., SCHLAGGAR, B. L. and PETERSEN, S. E. (2012). Spurious but systematic correlations in functional connectivity MRI networks arise from subject motion. *NeuroImage* **59** 2142–2154.
- RABIN, J., PEYRÉ, G., DELON, J. and BERNOT, M. (2011). Wasserstein barycenter and its application to texture mixing. In *International Conference on Scale Space and Variational Methods in Computer Vision* 435–446. Springer, Berlin.
- REININGHAUS, J., HUBER, S., BAUER, U. and KWITT, R. (2015). A stable multi-scale kernel for topological machine learning. In *Proceedings of the IEEE Conference on Computer Vision and Pattern Recognition* 4741–4748.
- REYNOLDS, C. A. and PHILLIPS, D. (2015). Genetics of brain aging—twin aging.
- ROBINS, V. and TURNER, K. (2016). Principal component analysis of persistent homology rank functions with case studies of spatial point patterns, sphere packing and colloids. *Phys. D* **334** 99–117. MR3545972 <https://doi.org/10.1016/j.physd.2016.03.007>
- ROTSCHY, C., LANGNER, R., DOGAN, I., REETZ, K., LAIRD, A. R., SCHULZ, J. B., FOX, P. T. and EICKHOFF, S. B. (2012). Modelling neural correlates of working memory: A coordinate-based meta-analysis. *NeuroImage* **60** 830–846.
- SAAD, D., ed. (1998). *On-Line Learning in Neural Networks. Publications of the Newton Institute* **17**. Cambridge Univ. Press, Cambridge. MR1763695
- SATTERTHWAITE, T. D., WOLF, D. H., LOUGHEAD, J., RUPAREL, K., ELLIOTT, M. A., HAKONARSON, H., GUR, R. C. and GUR, R. E. (2012). Impact of in-scanner head motion on multiple measures of functional connectivity: Relevance for studies of neurodevelopment in youth. *NeuroImage* **60** 623–632.
- SCHAEFER, A., KONG, R., GORDON, E. M., LAUMANN, T. O., ZUO, X. N., HOLMES, A. J., EICKHOFF, S. B. and YEO, B. T. T. (2017). Local-global parcellation of the human cerebral cortex from intrinsic functional connectivity MRI. *Cereb. Cortex* **28** 3095–3114.
- SCOTT, J. (1988). Social network analysis. *Sociology* **22** 109–127.
- SHAH, L. M., CRAMER, J. A., FERGUSON, M. A., BIRN, R. M. and ANDERSON, J. S. (2016). Reliability and reproducibility of individual differences in functional connectivity acquired during task and resting state. *Brain Behav.* **6** e00456.
- SHAPPELL, H. M., CAFFO, B. S., PEKAR, J. J. and LINDQUIST, M. (2019). Improved state change estimation in dynamic functional connectivity using hidden semi-Markov models. *NeuroImage* **191** 243–257.
- SHARATHKUMAR, R. and AGARWAL, P. K. (2012). Algorithms for the transportation problem in geometric settings. In *Proceedings of the Twenty-Third Annual ACM-SIAM Symposium on Discrete Algorithms* 306–317. ACM, New York. MR3205219
- SHATTUCK, D. W., MIRZA, M., ADISETIYO, V., HOJATKASHANI, C., SALAMON, G., NARR, K. L., POLDRACK, R. A., BILDER, R. M. and TOGA, A. W. (2008). Construction of a 3D probabilistic atlas of human cortical structures. *NeuroImage* **39** 1064–1080.
- SINGH, N., COUTURE, H. D., MARRON, J., PEROU, C. and NIETHAMMER, M. (2014). Topological descriptors of histology images. In *International Workshop on Machine Learning in Medical Imaging* 231–239. Springer, Berlin.
- SMIT, D. J. A., STAM, C. J., POSTHUMA, D., BOOMSMA, D. I. and DE GEUS, E. J. C. (2008). Heritability of small-world networks in the brain: A graph theoretical analysis of resting-state EEG functional connectivity. *Hum. Brain Mapp.* **29** 1368–1378.
- SMITH, R. E., TOURNIER, J. D., CALAMANTE, F. and CONNELLY, A. (2015). SIFT2: Enabling dense quantitative assessment of brain white matter connectivity using streamlines tractography. *NeuroImage* **119** 338–351.
- SNIJDERS, T., SPREEN, M. and ZWAAGSTRA, R. (1995). The use of multilevel modeling for analysing personal networks: Networks of cocaine users in an urban area. *J. Quant. Anthropol.* **5** 85–105.
- SONGDECHAKRAIWUT, T. and CHUNG, M. K. (2020). Dynamic topological data analysis for functional brain signals. In *2020 IEEE 17th International Symposium on Biomedical Imaging Workshops (ISBI Workshops)* 1–4. IEEE, New York.
- SONGDECHAKRAIWUT, T., KRAUSE, B. M., BANKS, M. I., NOURSKI, K. V. and VAN VEEN, B. D. (2022a). Topological classification in a Wasserstein distance based vector space. Preprint. Available at [arXiv:2202.01275](https://arxiv.org/abs/2202.01275).
- SONGDECHAKRAIWUT, T., KRAUSE, B. M., BANKS, M. I., NOURSKI, K. V. and VEEN, B. D. V. (2022b). Fast topological clustering with Wasserstein distance. In *International Conference on Learning Representations*.
- SONGDECHAKRAIWUT, T., SHEN, L. and CHUNG, M. K. (2021). Topological learning and its application to multimodal brain network integration. In *Medical Image Computing and Computer Assisted Intervention (MICCAI). Lecture Notes in Computer Science* **12902** 166–176.
- SPORNS, O. (2003). Graph Theory Methods for the Analysis of Neural Connectivity Patterns. In *Neuroscience Databases: A Practical Guide* 171–185. Springer, Boston, MA.

- TAYLOR, L. and NITSCHKE, G. (2018). Improving deep learning with generic data augmentation. In *2018 IEEE Symposium Series on Computational Intelligence (SSCI)* 1542–1547. IEEE, New York.
- TIAN, Y., YAN, J., ZHANG, H., ZHANG, Y., YANG, X. and ZHA, H. (2012). On the convergence of graph matching: Graduated assignment revisited. In *European Conference on Computer Vision* 821–835. Springer, Berlin.
- TOGA, A. W. and THOMPSON, P. M. (2003). Mapping brain asymmetry. *Nat. Rev. Neurosci.* **4** 37–48. <https://doi.org/10.1038/nrn1009>
- TOURNIER, J., CALAMANTE, F., CONNELLY, A. et al. (2012). MRtrix: Diffusion tractography in crossing fiber regions. *Int. J. Imaging Syst. Technol.* **22** 53–66.
- TURNER, K., MILEYKO, Y., MUKHERJEE, S. and HARER, J. (2014). Fréchet means for distributions of persistence diagrams. *Discrete Comput. Geom.* **52** 44–70. [MR3231030 https://doi.org/10.1007/s00454-014-9604-7](https://doi.org/10.1007/s00454-014-9604-7)
- TZOURIO-MAZOYER, N., LANDEAU, B., PAPHATHANASSIOU, D., CRIVELLO, F., ETARD, O., DELCROIX, N., MAZOYER, B. and JOLIOT, M. (2002). Automated anatomical labeling of activations in SPM using a macroscopic anatomical parcellation of the MNI MRI single-subject brain. *NeuroImage* **15** 273–289.
- VAN DIJK, K. R. A., SABUNCU, M. R. and BUCKNER, R. L. (2012). The influence of head motion on intrinsic functional connectivity MRI. *NeuroImage* **59** 431–438.
- VAN ESSEN, D. C., UGURBIL, K., AUERBACH, E., BARCH, D., BEHRENS, T., BUCHOLZ, R., CHANG, A., CHEN, L., CORBETTA, M. et al. (2012). The Human Connectome Project: A data acquisition perspective. *NeuroImage* **62** 2222–2231.
- VAN ESSEN, D. C., SMITH, S. M., BARCH, D. M., BEHRENS, T. E., YACCOUB, E., UGURBIL, K., CONSORTIUM, W.-M. H. et al. (2013). The WU-Minn human connectome project: An overview. *NeuroImage* **80** 62–79.
- WANG, Y., OMBAO, H. and CHUNG, M. K. (2018). Topological data analysis of single-trial electroencephalographic signals. *Ann. Appl. Stat.* **12** 1506–1534. [MR3852686 https://doi.org/10.1214/17-AOAS1119](https://doi.org/10.1214/17-AOAS1119)
- WANG, T., LIU, H., LI, Y., JIN, Y., HOU, X. and LING, H. (2020). Learning combinatorial solver for graph matching. In *Proceedings of the IEEE/CVF Conference on Computer Vision and Pattern Recognition* 7568–7577.
- WASSERMAN, L. (2018). Topological data analysis. *Annu. Rev. Stat. Appl.* **5** 501–535. [MR3774757 https://doi.org/10.1146/annurev-statistics-031017-100045](https://doi.org/10.1146/annurev-statistics-031017-100045)
- WIJK, B. C. M., STAM, C. J. and DAFFERTSHOFER, A. (2010). Comparing brain networks of different size and connectivity density using graph theory. *PLoS ONE* **5** e13701.
- XIA, K. and WEI, G.-W. (2014). Persistent homology analysis of protein structure, flexibility, and folding. *Int. J. Numer. Methods Biomed. Eng.* **30** 814–844. [MR3247713 https://doi.org/10.1002/cnm.2655](https://doi.org/10.1002/cnm.2655)
- XIE, L., AMICO, E., SALAMA, P., WU, Y. C., FANG, S., SPORNS, O., SAYKIN, A. J., GOŃI, J., YAN, J. et al. (2018). Heritability estimation of reliable connectomic features. In *International Workshop on Connectomics in Neuroimaging. Lecture Notes in Computer Science* **11083** 58–66.
- XUE, W., BOWMAN, F. D., PILEGGI, A. V. and MAYER, A. R. (2015). A multimodal approach for determining brain networks by jointly modeling functional and structural connectivity. *Front. Comput. Neurosci.* **9** 22. <https://doi.org/10.3389/fncom.2015.00022>
- YU, T., YAN, J., WANG, Y., LIU, W. et al. (2018). Generalizing graph matching beyond quadratic assignment model. In *Advances in Neural Information Processing Systems* 853–863.
- ZALESKY, A., FORNITO, A., HARDING, I. H., COCCHI, L., YÜCEL, M., PANTELIS, C. and BULLMORE, E. T. (2010). Whole-brain anatomical networks: Does the choice of nodes matter? *NeuroImage* **50** 970–983.
- ZAVLANOS, M. M. and PAPPAS, G. J. (2008). A dynamical systems approach to weighted graph matching. *Automatica J. IFAC* **44** 2817–2824. [MR2527202 https://doi.org/10.1016/j.automatica.2008.04.009](https://doi.org/10.1016/j.automatica.2008.04.009)
- ZEMEL, Y. and PANARETOS, V. M. (2019). Fréchet means and Procrustes analysis in Wasserstein space. *Bernoulli* **25** 932–976. [MR3920362 https://doi.org/10.3150/17-bej1009](https://doi.org/10.3150/17-bej1009)
- ZHANG, Z., DESCOTEAUX, M., ZHANG, J., GIRARD, G., CHAMBERLAND, M., DUNSON, D., SRIVASTAVA, A. and ZHU, H. (2018). Mapping population-based structural connectomes. *NeuroImage* **172** 130–145.
- ZHANG, G., CAI, B., ZHANG, A., STEPHEN, J. M., WILSON, T. W., CALHOUN, V. D. and WANG, Y. P. (2019a). Estimating dynamic functional brain connectivity with a sparse hidden Markov model. *IEEE Trans. Med. Imag.* **39** 488–498.
- ZHANG, Z., XIANG, Y., WU, L., XUE, B. and NEHORAI, A. (2019b). KerGM: Kernelized graph matching. In *Advances in Neural Information Processing Systems* 3335–3346.
- ZHOU, F. and DE LA TORRE, F. (2013). Deformable graph matching. In *Proceedings of the IEEE Conference on Computer Vision and Pattern Recognition* 2922–2929.
- ZHU, D., ZHANG, T., JIANG, X., HU, X., CHEN, H., YANG, N., LV, J., HAN, J., GUO, L. et al. (2014). Fusing DTI and fMRI data: A survey of methods and applications. *NeuroImage* **102** 184–191.